Cell Reports

Article

The endoplasmic reticulum kinase PERK interacts with the oxidoreductase ERO1 to metabolically adapt mitochondria

Graphical abstract

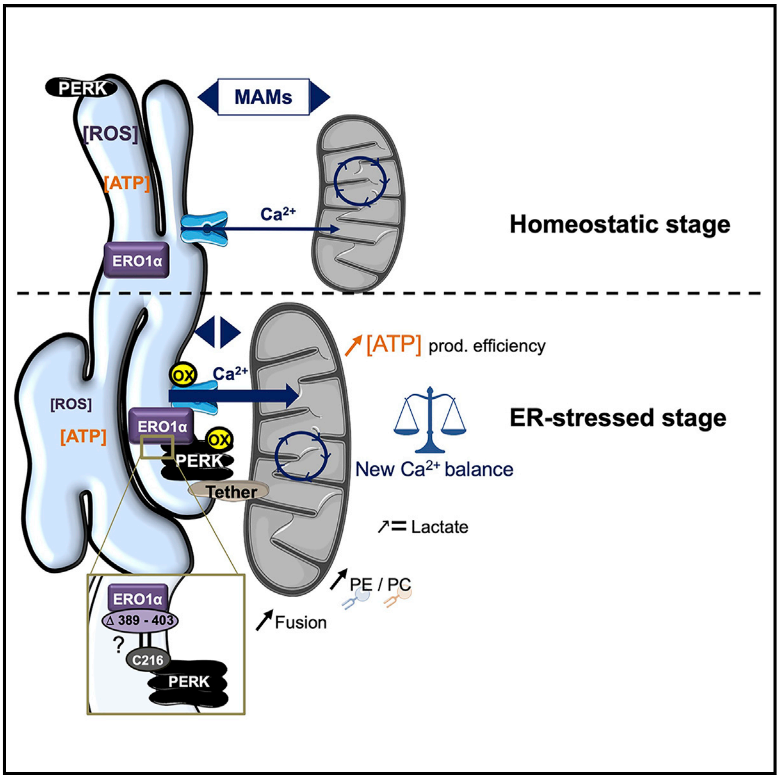

Highlights

- The ER oxidoreductase Ero1α binds to PERK during the early phases of ER stress
- The PERK-Ero1α complex increases mitochondria-ER contacts during early ER stress
- The PERK-Ero1α complex restores ER bioenergetics and moderates ROS levels

Authors

Arthur Bassot, Junsheng Chen,
Kei Takahashi-Yamashiro, ...,
Ivan Bogeski, Robert E. Campbell,
Thomas Simmen

Correspondence

thomas.simmen@ualberta.ca

In brief

During endoplasmic reticulum (ER) stress, the ER moves closer to mitochondria and activates bioenergetics. Bassot et al. show that a complex between Ero1α and the ER stress kinase PERK oxidizes key signaling proteins on mitochondria-ER contact sites (MERCs) and prevents energy depletion and oxidative stress within the ER and cytosol.

Bassot et al., 2023, Cell Reports *42*, 111899
January 31, 2023
https://doi.org/10.1016/j.celrep.2022.111899

CellPress

Cell Reports

CellPress
OPEN ACCESS

Article

The endoplasmic reticulum kinase PERK interacts with the oxidoreductase ERO1 to metabolically adapt mitochondria

Arthur Bassot,[1] Junsheng Chen,[1] Kei Takahashi-Yamashiro,[2] Megan C. Yap,[1] Christine Silvia Gibhardt,[7] Giang N.T. Le,[9] Saaya Hario,[9] Yusuke Nasu,[9] Jack Moore,[10] Tomas Gutiérrez,[1] Lucas Mina,[1] Heather Mast,[3] Audric Moses,[4] Rakesh Bhat,[11] Klaus Ballanyi,[5] Hélène Lemieux,[3] Roberto Sitia,[6] Ester Zito,[8,12] Ivan Bogeski,[7] Robert E. Campbell,[2,9] and Thomas Simmen[1,13,*]
[1]Department of Cell Biology, Faculty of Medicine and Dentistry, Edmonton, AB T6G 2G2, Canada
[2]Department of Chemistry, University of Alberta, Edmonton, AB T6G 2G2, Canada
[3]Faculty Saint-Jean, Department of Medicine, Faculty of Medicine and Dentistry, Edmonton, AB T6G2H7, Canada
[4]Department of Pediatrics, Edmonton, AB T6G2H7, Canada
[5]Department of Physiology, University of Alberta, Edmonton, AB T6G2H7, Canada
[6]Division of Genetics and Cell Biology, Università Vita-Salute IRCCS Ospedale San Raffaele, 20132 Milano, Italy
[7]Molecular Physiology, Institute of Cardiovascular Physiology, University Medical Center, Georg-August-University, Göttingen, Germany
[8]Istituto di Ricerche Farmacologiche Mario Negri, 20156 Milano, Italy
[9]Department of Chemistry, Graduate School of Science, The University of Tokyo, Bunkyo-ku, Tokyo 113-0033, Japan
[10]Alberta Proteomics and Mass Spectrometry Facility, University of Alberta, 4096 Katz Research Building, Edmonton AB T6G2E1, Canada
[11]Precision Biolaboratories, St. Albert, AB T8N 5A7, Canada
[12]Department of Biomolecular Sciences, University of Urbino Carlo Bo, 61029 Urbino PU, Italy
[13]Lead contact
*Correspondence: thomas.simmen@ualberta.ca
https://doi.org/10.1016/j.celrep.2022.111899

SUMMARY

Endoplasmic reticulum (ER) homeostasis requires molecular regulators that tailor mitochondrial bioenergetics to the needs of protein folding. For instance, calnexin maintains mitochondria metabolism and mitochondria-ER contacts (MERCs) through reactive oxygen species (ROS) from NADPH oxidase 4 (NOX4). However, induction of ER stress requires a quick molecular rewiring of mitochondria to adapt to new energy needs. This machinery is not characterized. We now show that the oxidoreductase ERO1α covalently interacts with protein kinase RNA-like ER kinase (PERK) upon treatment with tunicamycin. The PERK-ERO1α interaction requires the C-terminal active site of ERO1α and cysteine 216 of PERK. Moreover, we show that the PERK-ERO1α complex promotes oxidization of MERC proteins and controls mitochondrial dynamics. Using proteinaceous probes, we determined that these functions improve ER-mitochondria Ca^{2+} flux to maintain bioenergetics in both organelles, while limiting oxidative stress. Therefore, the PERK-ERO1α complex is a key molecular machinery that allows quick metabolic adaptation to ER stress.

INTRODUCTION

The endoplasmic reticulum (ER) uses oxidative protein folding to produce fully folded secretory proteins such as immunoglobulins and insulin.[1] This mechanism requires large amounts of adenosine trisphosphate (ATP),[2] defining the ER as one of the main cellular energy consumers.[3] ER Ca^{2+} is required for chaperones but can also transfer to mitochondria, where it maintains bioenergetics by controlling dehydrogenases of the Krebs cycle and oxidative phosphorylation (OXPHOS).[4] This effect is at the basis of an increased formation of mitochondria-ER contacts (MERCs) upon ER stress.[5] A central question is how the ER mechanistically achieves this plastic interaction with mitochondria to maintain its bioenergetics.

A machinery mediating metabolic interaction of the ER with mitochondria should localize to MERCs. This type of membrane contact sites (MCSs) was discovered on electron micrographs[6] and can be biochemically isolated as mitochondria-associated membranes (MAMs).[7,8] MAMs are lipid-metabolizing centers[9] and act as important sites of lipid synthesis and transfer.[10] This function is reflected by the recent description of a rough ER membrane domain enriched in lipid-metabolizing enzymes wrapped around mitochondria (wrappER) in liver tissue.[11] However, MAMs also serve as a Ca^{2+} conduit toward mitochondria.[12] Within MAMs, Ca^{2+} is released by inositol 1,4,5 trisphosphate receptors (IP_3Rs), which can also act as physical tethers[13] through interactions with voltage-dependent anion-specific channels (VDAC) and the mitochondrial chaperone Grp75.[14] This MERC-localized IP_3R function is needed to maintain mitochondrial OXPHOS,[15] thus favoring cell survival.[16] NADPH oxidase 4 (NOX4), an ER-localized producer of reactive oxygen species (ROS), provides a baseline oxidation of IP_3Rs that is necessary for OXPHOS.[17] However, mitochondrial ROS can leak into the MERC cleft.[18] In addition to a mitochondrial origin,[19] ROS-based signals also originate in the ER and act through IP_3Rs oxidation.[20] Such signals can be transmitted by aquaporin-11.[21] This peroxiporin is also used by mitochondrial ROS upon interference with ER protein folding,[22] a mechanism that requires mitofusin-2 (Mfn2).[23] However, ER stress eventually leads to a reduction of the ER oxidative environment,[24] and this change reduces Ca^{2+} release due to the replacement of IP_3R1-stabilizing proteins such as immunoglobulin binding protein (BiP/Grp78) with IP_3R1-inhibiting proteins such as ERp44.[25] The synthesis of these findings suggests that ROS-mediated control of ER homeostasis is not yet completely understood.

Like NOX4, the two human ER oxidoredoxins ERO1α and β produce ROS.[26,27] ERO1α localizes to MERCs,[28] from where it activates mitochondrial Ca^{2+} import by the mitochondrial Ca^{2+} uniporter (MCU).[29] The oxidizing activity of ERO1 is counteracted by ER peroxidases, such as peroxiredoxin 4 (Prx4), as well as the glutathione peroxidases GPx7 and GPx8, which prevent H_2O_2 leakage.[30,31] Moreover, the ER chaperone calnexin uses ROS signaling derived from both ERO1 and NOX4 to control ER Ca^{2+} filling by sarco-ER Ca^{2+} ATPase (SERCA).[32] These findings suggest that NOX4 or ERO1 enzymes could be part of the adaptive phase of ER stress/MERC signaling that aims to re-establish ER bioenergetics required for chaperones such as BiP/GRP78 during a folding crisis. According to this hypothesis, redox enzymes could trigger the post-translational modification (PTM) of proteinaceous tethers between the ER and mitochondria, such as Mfn2,[33] or vesicle-associated membrane protein-associated protein B (VAPB).[34,35] Alternatively, ER stress could modify the inositol-requiring enzyme 1 (Ire1) or the protein kinase RNA-like ER kinase (PERK) that both moonlight as MERC tethers. Ire1 controls ER-mitochondria Ca^{2+} transfer to maintain energy homeostasis.[36] Similarly, PERK promotes ER-mitochondria contact points[37] and propagates ROS signals toward mitochondria[38] upon its oligomerization.[39] Moreover, PERK phosphorylates the eukaryotic initiation factor 2α (eIF2α), which increases production of the mitochondrial supercomplex activation factor 1 (SCAF1).[40] Such long-term ER stress, as observed during obesity, increases MERCs but reduces OXPHOS due to mitochondrial Ca^{2+} overload.[41] While long-term MERC changes have been well described, molecular mechanisms allowing for quick metabolic adjustments and mitochondria activation[5] are not known. Here, we provide evidence that MERC-localized PERK interacts with ERO1α during a phase of the ER stress response when the ER folding environment must adapt to allow for the increased demand of energy-consuming chaperones, to increase MERCs and restore ER and mitochondrial bioenergetics.

RESULTS

PERK and ERO1α interact on MERCs upon ER stress

In addition to their well-characterized function in the unfolded protein response (UPR), the transmembrane ER stress sensors Ire1 and PERK signal to mitochondria. While Ire1 controls homeostatic bioenergetics,[36] long-term ER stress uses PERK to deliver apoptotic signals to mitochondria.[37,38] However, ER stress changes the ER oxidative poise[24,42] and activates mitochondria in a much shorter time frame.[5] We hypothesized that such an uncharacterized mechanism requires PERK rather than Ire1 and that it could be based on interactions with ER oxidoreductases or chaperones before the induction of the pro-apoptotic C/EBP homologous protein (CHOP). Thus, we used an unbiased mass-spectrometric approach (see https://repository.jpostdb.org/entry/JPST001942), where we isolated the interactome of FLAG-tagged PERK from control HEK293 cells and from cells exposed to 1 h of tunicamycin. As expected, we detected decreasing amounts of BiP/Grp78 but increasing amounts of the PERK substrate eIF2α at this time point (Figure 1A). Proteins such as Rrbp1 that mediate lipid metabolic interaction of the rough ER with mitochondria were not detected.[11] Among the interacting ER redox proteome, we detected small changes for ERp44, ERp72, and ERp57, but a large increase for ERO1α. This was intriguing, because ERO1α is a potential ROS source.

Next, we biochemically fractionated cellular homogenates with the classic Percoll gradient protocol that separates MAMs from mitochondria.[9] Upon 1 h of tunicamycin treatment, we found that PERK increased within MAMs, while Ire1α did so to a lesser extent (Figure 1B). We replicated the fractionation in PERK knockout (KO) mouse embryonic fibroblasts (MEFs). This showed that Ire1α continued to move onto MAMs in these cells, suggesting its MAM enrichment does not depend on PERK. We found a very different behavior when analyzing ER redox enzymes and ROS sources. ERO1α, NOX4, PDI, and Prx4 showed robust increases on MAMs in wild-type (WT) MEFs. In contrast, the moieties of these MAM-associated enzymes did not change in PERK KO cells (Figure 1B). We were able to confirm proximity between PERK and ERO1α after 1 h of tunicamycin-mediated ER stress with an increased Manders coefficient between endogenous PERK and ERO1α (Figure 1C). Similarly, ER heavy (MAMs and mitochondria) and light membranes (microsomes, smooth ER)[43] from WT MEFs showed that endogenous PERK and Ire1α reached maximal signals on MAM-containing heavy membranes after 1 h of ER stress (Figure S1A). Here, they cofractionate with MAM markers such as Grp75 and encounter the ROS source ERO1α, but not NOX4, coinciding with increased proximity between endogenous ERO1α and mitochondria in HeLa cells (Figure S1B). Thus, we hypothesized that PERK could anchor the redox-regulatory enzymes ERO1α, NOX4, PDI, and Prx4 on MAMs. Due to the well-known role of PERK in the induction of apoptosis, we first tested apoptotic readouts at the time point when we detected co-localization between PERK and ERO1α. We confirmed the absence of positive Annexin V and propidium iodide staining at 1 h of tunicamycin treatment (Figure 1D). Next, we confirmed that the induction of the apoptotic CHOP did not occur at 1 h of tunicamycin treatment (Figure S1C). Thus, 1 h of tunicamycin treatment coincides with the enrichment of PERK and ER redox enzymes at MERCs during the early phases of ER stress but does not coincide with apoptosis.

Next, we investigated the dynamics and cause of this apposition between PERK and ER redox enzymes. Thus, we immunoprecipitated FLAG-tagged PERK and quantified associated ERO1α, Prx4 as well as the MAM-tethering protein Mfn2, in HEK293 cells. This showed that PERK interacted best with

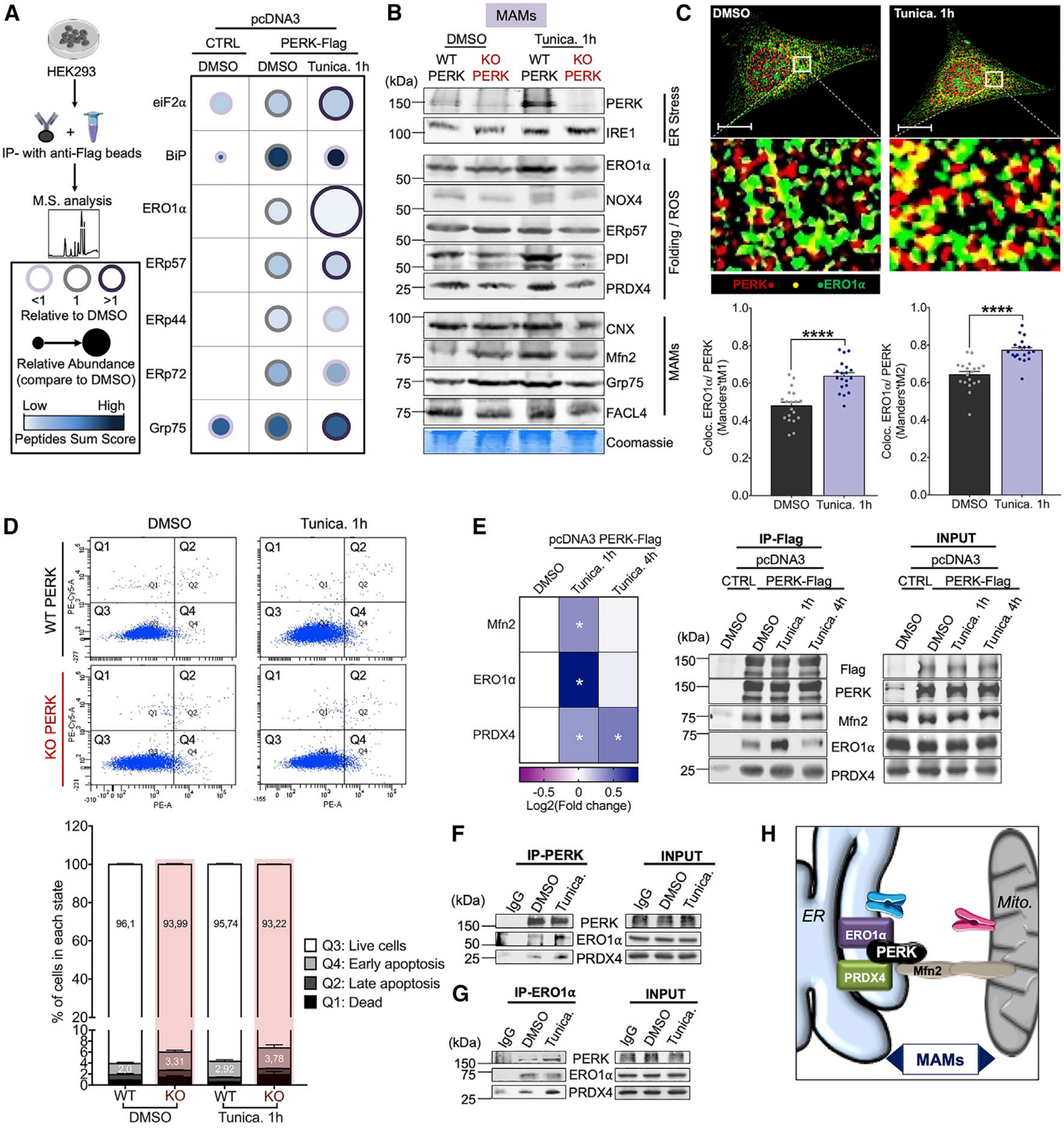

Figure 1. PERK and ERO1α interaction and distribution during ER stress

All data are presented as mean ± standard error of the mean.

(A) Mass spectrometry of FLAG immunoprecipitates. Peak areas of indicated proteins are expressed as fold increase compared with the control (normalized at 1) from HEK293 cells expressing PERK-FLAG (treated with 10 μg/mL of tunicamycin for 1 h).

(B) MAM isolates after fractionation protocol following treatment as in (A) (representative of n = 3 technical replicates).

(C) Co-localization of endogenous ERO1α and PERK during ER stress in control and ER-stressed HeLa cells. Manders coefficients indicate PERK overlapping with ERO1α (Manders' tM2) or ERO1α overlapping with PERK (Manders' tM2) (n = 19 cells/condition in n = 2 biological replicates, ****$p < 0,0001$, unpaired t test). Scale bars: 20 μM.

(D) Apoptosis analysis. Cells treated as in (B) were analyzed for Annexin V and phosphatidylinositol (PI) as indicated (n = 9–10 biological replicates for each group; Fisher multiple comparison following two-way ANOVA).

(E) Analysis of PERK-FLAG immunoprecipitates from HEK293 cells treated as in (A). Inputs (4%, right) and cross-linked lysates of FLAG immunoprecipitates (IP-FLAG, left) were analyzed for Mfn2, Grp75, ERO1α, and Prx4 (heatmap, right; n = 3–13 biological replicates, *$p < 0.05$, unpaired t test).

(F and G) Endogenous PERK and ERO1α immunoprecipitation. HEK293 cells were treated as in (A). Immunoprecipitates (ERO1α and PERK) and inputs (4%, right) were analyzed for PERK, ERO1α, and Prx4 (n = 2 biological replicates).

(H) Model.

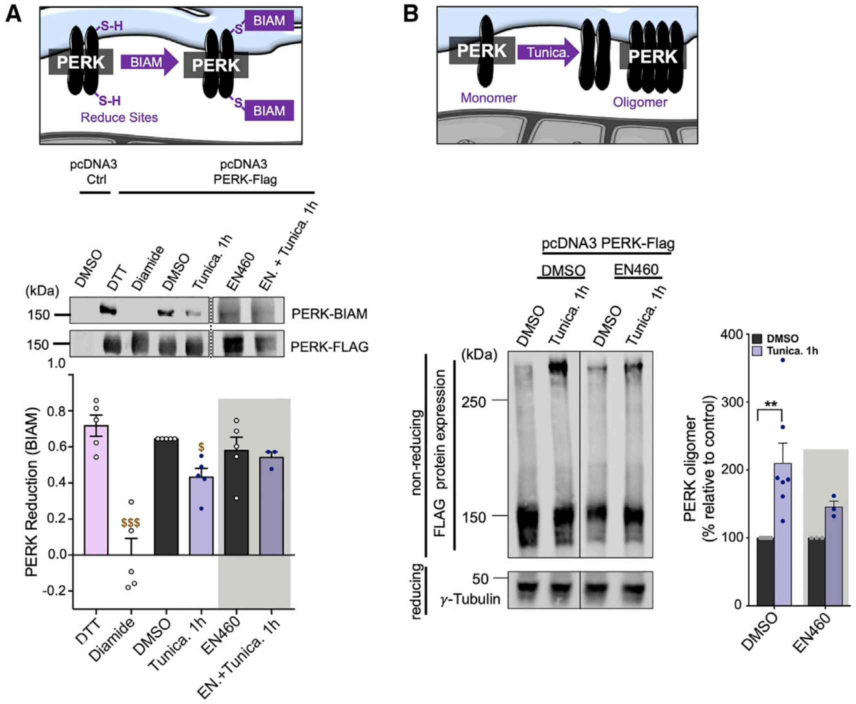

Figure 2. ERO1α oxidizes PERK upon ER stress

All data are presented as mean ± standard error of the mean.

(A) PERK BIAM analysis in HEK293 cells. Cells transfected with pcDNA3 or pcDNA3-PERK-FLAG were treated with DTT (10 mM), diamide (5 mM, 10min), and tunicamycin (10 μg/mL, 1h) following 25 μM EN460 (16h) or DMSO. Relative BIAM signals were normalized to DMSO (n = 3–5 biological replicates, \$p < 0.05; \$\$\$p < 0.001 by uncorrected Dunn's tests).

(B) Detection of SDS-resistant PERK oligomers during ER stress (10 μg/mL tunicamycin, 1 h). HEK293 cells were treated as in (A). Lysates were analyzed on non-reducing gels. Western blot membranes were analyzed for FLAG (left, top) and γ-tubulin (left, bottom) as indicated (n = 3–7 biological replicates; **p < 0.01 Bonferroni multiple comparison following two-way ANOVA).

ERO1α at 1 h of ER stress (Figure 1E), while this interaction decreased subsequently (Figure S1D). The PERK-ERO1α interaction was also detected with endogenous PERK (Figure 1F) and ERO1α (Figure 1G) or between myc-tagged ERO1α and endogenous PERK (Figure S1E). The PERK interaction with ERO1α increased in parallel with PDI or Prx4, as well as with Mfn2 (Figure S1D). We next examined this effect with another ER stressor. We chose to use thapsigargin. This showed that the depletion of ER Ca^{2+} also caused a PERK-ERO1α co-immunoprecipitate, albeit at 4 h (Figure S1F). These time differences could be drug or dosage dependent. We determined that tunicamycin started showing PERK-ERO1α co-immunoprecipitation at 0.5 μg/mL, while this happened at 0.5 μM thapsigargin (Figure S1G). We further investigated what triggered the two proteins to interact by incubating with the protein translation inhibitor cycloheximide to mimic an arrest of protein synthesis. This reduced the ERO1α signal associated with PERK (Figure S1G). In contrast, depletion of cellular glutathione by buthionine sulfoximine (BSO) or general oxidation with diamide increased the interaction (Figure S1H). No such increase could be detected between ERO1α and Ire1α (Figure S1I), although this UPR sensor did show increased interaction with the MERC tether Grp75, as published.[36] Moreover, we were unable to detect increased interaction between PERK and NOX4 (Figure S1J). Therefore, ER stress of various kinds leads to the specific formation of a PERK-ERO1α complex before the induction of apoptotic markers (Figure 1H).

ERO1α mediates oxidation of PERK upon ER stress

Next, we investigated the significance of the PERK-ERO1α interaction. A complex between the two could affect oxidative PTMs locally, as also observed in calnexin KO cells that show reduced oxidation of Ca^{2+} handling proteins due to inactivity of NOX4 and ERO1α[32]. We investigated the oxidation state of PERK with biotinylated iodoacetamide (BIAM) labeling during ER stress (Figure 2A). This showed that PERK was initially mostly reduced. However, upon ER stress, PERK became oxidized. Next, we tested whether the ERO1 enzymatic activities could be required for this modification by using the general ERO1 inhibitor EN460.[44] We determined that we could detect neither increased ERO1α interaction (Figure S2A) nor PERK oxidation in that case (Figure 2A). Moreover, PERK oxidation did not occur in ERO1α KO MEFs either (Figure S2B). Next, we tested if this oxidation resulted in PERK dimerization (Figure 2B), which occurs independent of the UPR.[39] Indeed, we could detect high-molecular-weight species following 1 h of tunicamycin treatment for transfected FLAG-tagged PERK (Figure 2B) and endogenous PERK (Figure S2C). Moreover, their formation was sensitive to ERO1 inhibition (Figure 2B), genetic KO of ERO1α (Figure S2D), and RNAi-mediated knockdown of ERO1α (Figure S2E). In sharp contrast with long-term ER stress, which usually induces activating transcription factor 4 (ATF4) and CHOP,[40,41] this observation coincided with active eIF2α but neither CHOP nor apoptosis induction. However, EN460 incubation reduced the typical readouts of PERK activation (Figure S2F). Therefore, interaction between PERK and ERO1α is accompanied by ERO1-dependent oxidation and oligomerization of PERK during the early phases of ER stress.

ERO1α and PERK cooperate to fuse mitochondria and tighten MERCs

To characterize the molecular mechanism based on PERK oxidation and on PERK-ERO1α interaction, we next quantified MERCs on electron micrographs of PERK and ERO1α WT and KO MEFs (Figure 3A). This showed that, in WT cells, MERCs tightened upon ER stress. In sharp contrast, such a shift from

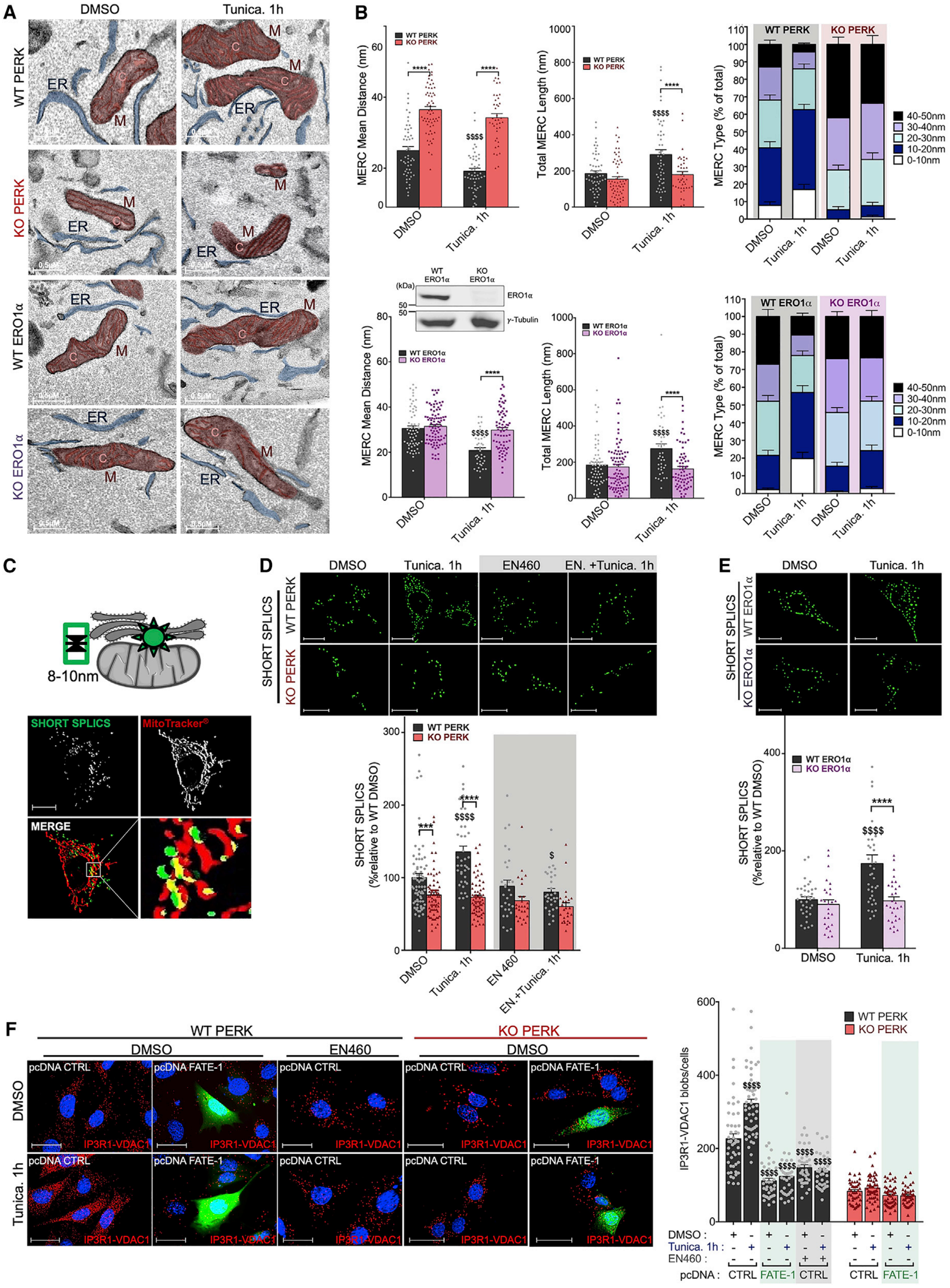

(legend on next page)

long-distance MERCs to short-distance MERCs was not observed in PERK or ERO1α KO MEFs (Figure 3B). We confirmed this behavior by a split GFP-based contact site sensor (SPLICS, Figure 3C).[45,46] This sensor protein showed an increase of short-distance MERCs in WT MEFs that was not observed in KO PERK MEFs (Figure 3D) or ERO1α KO MEFs (Figure 3E). The ERO1 inhibitor EN460 also abolished this change (Figure 3D). No changes were observed regarding long-distance MERCs in PERK or ERO1α KO MEFs upon tunicamycin treatment (Figures S3A and S3B). As expected, transfection of a MERC spacer (FATE-1[47]), also prevented these structural changes (Figure 3F). In parallel, the mitochondrial network underwent fusion in an ERO1-dependent manner (Figures S3C and S3D). These results demonstrate that MERCs increase upon interaction between PERK and ERO1α.

MERC remodeling could prompt PERK and ERO1α to alter lipid metabolism. We measured the lipid content of PERK WT and KO MEFs and did not detect major differences for phosphatidylserine (PS) (Figures S3E and S3F). In contrast, decreases of phosphatidylethanolamine (PE) and phosphatidylcholine (PC) appeared in PERK KO MEFs. Thus, we focused on the amounts of these lipids in our ER stress time course. However, while ER stress boosted the presence of PE and PC in PERK WT MEFs or upon ERO1 inhibition, this was not observed when both were disrupted (Figures S3G and S3H). Our results therefore suggested that PERK cooperates with ERO1 to increase PE and PC during early ER stress.

ERO1α and PERK work together to boost Ca^{2+} flux and mitochondrial bioenergetics during ER stress

The oxidation of PERK by ERO1α could occur in parallel with the oxidation of Ca^{2+} handling proteins. One candidate is SERCA2b, which is kept active and partially oxidized by the ER chaperone calnexin in a NOX4/ERO1-dependent manner.[32] During ER stress, SERCA2b oxidation increased (Figure S4A). Thus, we measured free ER Ca^{2+} with the ER-RGECO indicator[48] in the presence of the tert-Bu-BHQ (tBHQ) SERCA inhibitor (Figure S4B). In this setup, ERO1-inhibition by EN460 as well as ER stress mediated a modest 25% decrease of the ER Ca^{2+} content in PERK WT MEFs but not KO MEFs (Figures S4C and S4D). To investigate the significance of this change, we also measured cytosolic Ca^{2+} (Figure S4E). Here, we observed slightly increased Ca^{2+} clearance upon ER stress that was not observed upon ERO1 inhibition (Figures S4F and S4G). Therefore, the contribution of ERO1α to SERCA activity is highest during ER stress.

In addition to these SERCA-derived effects, ER stress increased IP_3R-mediated Ca^{2+} release in PERK WT MEFs that was attenuated by ERO1 inhibition (Figures S4F and S4G). Thus, we investigated IP_3R1 oxidation that is known to increase when activated.[25] Indeed, ER stress led to the oxidation of IP_3R1, but this effect was abolished upon inhibition of ERO1. In contrast, NOX4 inhibition did not result in a trend (Figure 4A). As expected from a role of PERK and ERO1α in IP_3R1 oxidation, this effect was attenuated in PERK KO MEFs and abolished in ERO1α KO MEFs (Figures 4B and 4C). Together, our results suggested that ER stress caused ERO1α to activate SERCA as well as IP_3R-mediated Ca^{2+} release through oxidation in a PERK-dependent manner.

Next, we hypothesized that this increased cytosolic Ca^{2+} signal could allow PERK to use the ERO1 enzymatic activity to also strengthen mitochondrial Ca^{2+} signals. Thus, we quantified Ca^{2+} signaling toward mitochondria with the Mito-RGECO probe (Figure 4C).[48] In WT cells, ER stress allows IP_3Rs to transfer more Ca^{2+} to mitochondria. However, this boosted signal was not observed in PERK KO MEFs or upon ERO1 inhibition (Figures 4E and 4F). This role of ERO1 was also observed in HeLa cells (Figure S5A). PERK/ERO1 signaling started immediately after triggering ER stress (Figure 4G). The Ca^{2+} burst was decreased by ERO1 inhibition in KO MEFs by about 20% and eliminated by the absence of PERK, which reduced the overall signal by about 40% (Figure 4G). This provided further evidence that PERK controls the contribution of ERO1α to fast Ca^{2+} signaling. Next, we blocked mitochondrial Ca^{2+} import with *p*-[trifluoromethoxyl]-phenyl-hydrazone (FCCP) to estimate mitochondrial $[Ca^{2+}]$.[49] This showed that, following an initial increase in mitochondrial $[Ca^{2+}]$, the mitochondrial $[Ca^{2+}]$ only showed a minor reduction after 1 h of tunicamycin treatment in WT MEFs (Figures S5B–S5D). However, if Ca^{2+} was removed from the growth medium, this effect was accentuated (Figure S5E and S5F). Taken together, PERK and ERO1α cooperate to increase ER-mitochondria Ca^{2+} transfer upon tunicamycin treatment.

These findings indicated that PERK could use ERO1α to control the adaptation of mitochondria metabolism to ER stress. This hypothesis was supported by an increase of the mitochondrial membrane potential upon ER stress-mediated interaction between PERK and ERO1α (Figure 4I). Moreover, when measuring

Figure 3. ERO1α and PERK control MERCs upon ER stress

All data are presented as mean ± standard error of the mean.

(A) Electron microscopy (EM) images from PERK/ERO1α KO and WT MEFs treated with tunicamycin (10 μg/mL) or DMSO for 1 h. Scale bar: 500 nm.

(B) EM quantifications. Average ER-mitochondria (MERC) distance (left), total MERC length (middle), and MERC distance distribution (right, as indicated). n = 51–53 MERC analyzed for PERK WT DMSO/1 h tunicamycin; n = 40–61 MERC analyzed for PERK KO DMSO/1 h tunicamycin; n = 39–63 MERC analyzed for ERO1α WT DMSO/1 h tunicamycin; n = 71–90 MERC analyzed for ERO1α KO DMSO/1 h tunicamycin in n = 3 technical replicates; statistics: $$$$ or ####p < 0.0001; compared with WT ($) or KO (#) under DMSO conditions; Bonferroni multiple comparison following two-way ANOVA, and ****p < 0.0001 Bonferroni multiple comparison between WT and KO following two-way ANOVA.

(C) Model for short SPLICS (MERC distance: 8–10 nm).

(D and E) Images of short SPLICS of PERK WT and KO MEFs (D, top) and ERO1α WT and KO MEFs (E, top) from cells treated as in (A) following 25 μM EN460 or DMSO (16 h). Scale bars: 20 μm. Quantification (bottom). (D) n = 24–73 cells per condition and (E) n = 27–37 cells in n = 3 biological replicates per condition, $ or #p < 0.05 and $$$$ or ####p < 0.0001 compared with WT ($) or KO (#) under DMSO conditions; Statistics: Bonferroni multiple comparison following two-way ANOVA; and *p < 0.05; ***p < 0.001; ****p < 0.0001. Scale bars: 20 μm.

(F) PLA images for IP_3R and VDAC1 from PERK WT and KO MEFs transfected with pcDNA3 control or FATE-1. n = 35–55 cells in n = 3 biological replicates per condition, $ or #p < 0.05 and $$$$ or ####p < 0.0001 respectively compared with WT ($) or KO (#) under DMSO conditions. Scale bars: 20 μm.

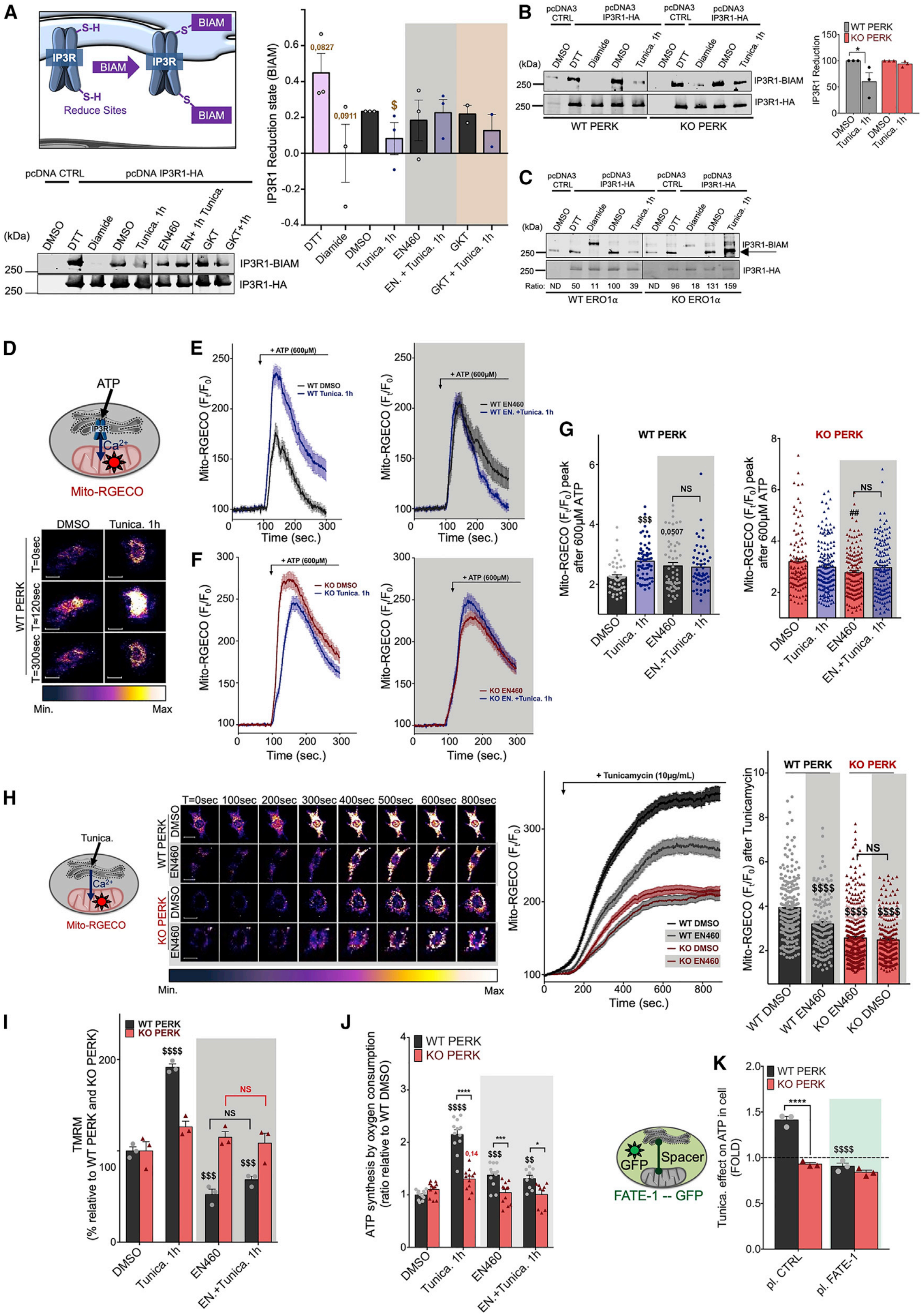

(legend on next page)

ATP relative to oxygen consumption in PERK WT and KO MEFs, we found that tunicamycin-induced ER stress improved mitochondrial bioenergetics. This was not seen in KO MEFs or upon inhibition of ERO1 (Figure 4J) and did not depend on NOX4 (Figure S5G). Upon a block of MERC tightening, we failed to detect ER stress-dependent changes in ATP (Figure 4K). As expected from higher tetramethylrhodamine methyl ester (TMRM) signals, ER stress did not increase respiration in our cells (Figure S5H), suggesting PERK WT cells enter a state where they produce more ATP but use less oxygen.[50] In contrast, PERK KO MEFs had overall less oxygen consumption that remained stable (Figure S5H). This finding could be largely replicated with PERK knockdown for the respiratory uncoupled state in HEK293 cells (Figure S5I).

During ER stress, interaction between ERO1α and PERK maintains homeostasis

Given mitochondrial bioenergetics were maintained during a short-term tunicamycin-induced ER stress and required the presence of both PERK and ERO1α, we next investigated several key readouts of ER and mitochondria homeostasis. First, we tested whether increased energy production within mitochondria could also maintain ATP levels within the ER lumen. These are critical for the functioning of ER chaperones during ER stress.[51] Consistent with a role of both PERK and ERO1α, ATP levels dropped within the ER when we interfered with either one but remained stable when both were present (Figures 5A–5C). Next, we investigated the significance of PERK and ERO1α for the cellular redox poise. ER peroxidases scavenge ERO1-derived H_2O_2,[30,31] and these ROS can show a mild increase during ER stress[42] or a decrease.[24] These opposing consequences could be determined by the relative abundance of ER redox enzymes as seen in different central nervous system cell types.[52] Using an ER-targeted roGFP2 redox sensor (Figure 5D),[53,54] we determined that, in PERK KO MEFs, the ER was more oxidizing, in an ERO1-dependent manner (Figure 5E). While under control conditions, this signal was stable (Figure S6A), a short-term tunicamycin treatment caused a mild reduction of the ER in our MEFs (Figure 5F). Importantly, this did not occur upon inhibition of ERO1.

Our findings so far indicated that early tunicamycin treatment caused the oxidation of key MERC signaling proteins PERK, SERCA, and IP_3Rs (Figures 2A, 2B, 4A–4C, S2B–S2E, and S4A), but did not promote cell death (Figures 1D, S2F, and S2G). To further investigate how PERK and ERO1α use these proteins to rewire mitochondrial and ER bioenergetics without causing overall ER hyperoxidation during early tunicamycin-induced ER stress, we measured ROS on multiple additional locations. First, we measured overall ROS levels that we assayed with MitoSOX inside mitochondria (Figure S6B) and with CellROX, measuring total ROS (Figures 5G, S6C, and S6D). Both signals also specifically decreased during ER stress in a PERK and ERO1α-dependent manner. Importantly, locking MERCs into a wider distance with FATE-1 removed PERK and ERO1-mediated effects on mitochondrial ROS but not total cellular ROS, since only a decrease of CellROX remained visible in cells where we had locked in MERCs at a wider distance (Figure S6E).

We further investigated this hypothesis by measuring H_2O_2 on the outer mitochondrial membrane (OMM). Like MitoSOX, this assay showed decreased signals from the OMM-HyPer construct at the OMM after 1 h of ER stress in an ERO1-dependent manner in PERK WT cells. Therefore, inhibition of the ERO1 enzymatic activity restored ROS levels in PERK KO cells but also removed their ER stress-related decrease in the cytoplasm or mitochondria of PERK WT cells. This suggested that the sequestration of ERO1 by PERK causes the local oxidation of MERC proteins, but globally reduces ER and mitochondria ROS levels.

Figure 4. PERK-ERO1α controls ER-mitochondria Ca^{2+} flux, Ca^{2+} handling protein oxidation, and mitochondria metabolism

All data are presented as mean ± standard error of the mean.

(A) IP_3R1 BIAM analysis in HEK293 cells. Cells transfected with pcDNA3-IP_3R1-HA or a control plasmid were treated as indicated (see Figure 2A) and analyzed for HA and BIAM signals with the diamide signal set at 0 (n = 3 biological replicates for each group, \$p < 0.05 compared with DTT; Dunn's multiple comparison following Kruskal-Wallis).

(B and C) IP_3R1 BIAM analysis in PERK (B)/ERO1α (C) WT and KO MEFs (B left and C) and quantification (B, right) (B, n = 3 biological replicates, *p < 0.05 compared with DMSO; unpaired t test/C, n = 1 biological replicate).

(D) Diagram illustrating the Mito-RGECO Ca^{2+} sensor and images as indicated.

(E and F) Average curve profiles in PERK WT (E) and KO (F) MEFs.

(G) ER-Mitochondrial Ca^{2+} transfer measurements. PERK WT (left) and KO (right) MEFs transfected with Mito-RGECO were treated as indicated (see Figure 2A) and average peaks were quantified. n = 45–163 cells in n = 4–6 biological replicates per condition, \$\$ or ##p < 0.01; \$\$\$ or ###p < 0.001 respectively compared with WT (\$) or KO (#) DMSO; Bonferroni multiple comparison following one-way ANOVA. Scale bars: 20 μm.

(H) (Left) Diagram and (center) Mitochondrial Ca^{2+} uptake during ER stress. Movie stills from a tunicamycin time course (10 μg/mL) in PERK WT and KO MEFs, using Mito-RGECO. Scale bars: 20 μm. (Right) Quantification of mitochondrial Ca^{2+} uptake during ER stress. PERK WT and KO MEFs were transfected, treated as indicated (see Figure 2A) and imaged (n = 141–396 cells in n = 7–8 biological replicates per condition, \$\$\$\$p < 0.0001 between each condition; Bonferroni multiple comparison following one-way ANOVA).

(I) Mitochondrial membrane potential. PERK WT and KO MEFs were treated as in Figure 2A, loaded with TMRM, and processed for flow cytometry (n = 3 biological replicates by condition, \$\$\$ or ###p < 0.001 and \$\$\$\$ or ####p < 0.0001 respectively compared with WT (\$) or KO (#) DMSO; Bonferroni multiple comparison following one-way ANOVA).

(J) Total cellular ATP content. ATP was quantified relative to the oxygen consumption and normalized as percentage relative to the PERK WT DMSO condition from cells treated as indicated (see Figure 2A). n = 6–12 biological replicates per condition, \$\$ or ##p < 0.01; \$\$\$ or ###p < 0.001, and \$\$\$\$ or ####p < 0.0001 respectively compared with WT (\$) or KO (#) DMSO; Bonferroni multiple comparison following two-way ANOVA and *p < 0.05; **p < 0.01, and ****p < 0.0001 Bonferroni multiple comparison following two-way ANOVA.

(K) Total cellular ATP content per microgram of protein in cells transfected with pcDNA control or FATE-1 treated as indicated (see Figure 2A). n = 3 biological replicates per condition, \$\$\$\$ or ####p < 0.0001 respectively compared with WT (\$) or KO (#) pcDNA control; Bonferroni multiple comparison following two-way ANOVA and ****p < 0.0001 Bonferroni multiple comparison between PERK WT and KO following two-way ANOVA.

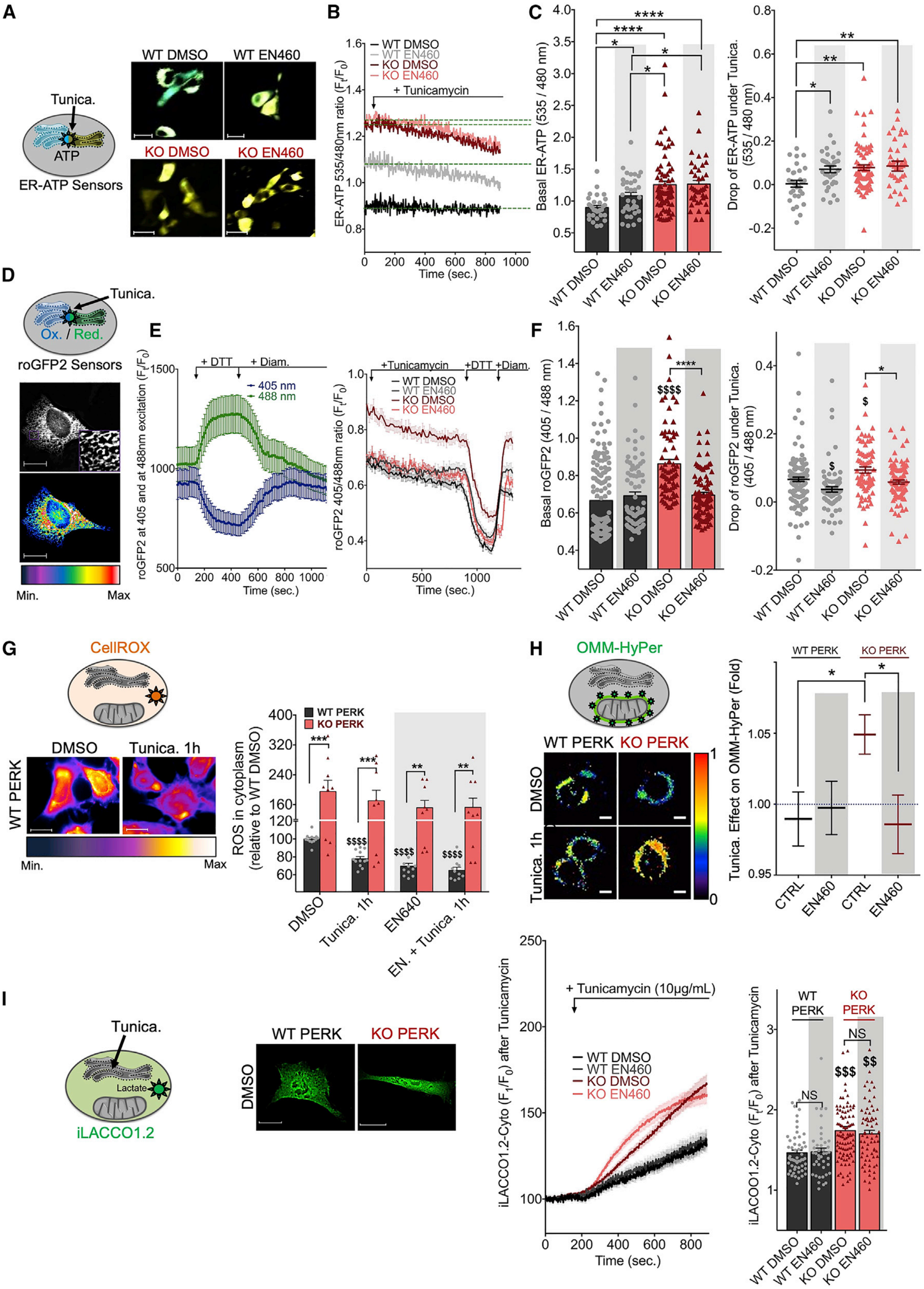

(legend on next page)

Last, we investigated whether ERO1 also influences glycolysis in the expectation that a disruption of mitochondrial bioenergetics would result in increased L-lactate intracellularly upon ER stress (Figure 5I) or in the growth medium (Figure S6F). Intracellular L-lactate was measured with a novel genetically encoded L-lactate biosensor, iLACCO1.2 ($\Delta F/F_o \sim 18$ and $K_{D,app} \sim 35\ \mu M$ *in vitro*). This probe detected increased production of L-lactate in PERK KO cells overall and following short-term tunicamycin treatment regardless of ERO1 (Figure 5I). In contrast, ER stress caused L-lactate in the medium to increase upon interference with ERO1 in the presence of PERK (Figure S6F), but we could not detect an ER stress-dependent L-lactate increase in the medium in the absence of PERK that resulted in overall lower medium pH (Figure S6G). This suggested that PERK and ERO1 repress glycolysis globally but ER stress only boosts glycolysis if both ERO1 and PERK are inhibited. These results mirrored the decreased respiration triggered by ER stress that also was only ERO1 dependent in the presence of PERK. Together, upon ER stress, a combined effect of PERK and ERO1 on L-lactate was detected in the medium, while intracellular L-lactate levels were only connected to PERK.

Therefore, our data so far indicated that PERK KO cells do not make use of ERO1 to adapt their bioenergetics within the ER and mitochondria during ER stress and react by increasing ROS on the OMM and L-lactate production. In contrast, WT cells oxidize MERC proteins, coinciding with PERK-ERO1α interaction, in order to achieve a new metabolic equilibrium.

PERK Cys216 and an ERO1α active site form a covalent complex

To test the possible role of PERK and ERO1α in the maintenance of mitochondrial and ER bioenergetics further (Figure 6A), we first constructed a kinase-dead (F927H) and three cytoplasmic PERK deletion mutants (Δ593-1116, Δ678-1116, Δ865-1116) (Figure 6B). This aimed to test whether PERK kinase activity is required for the capturing of ERO1α during ER stress. None of these mutants abolished the increased interaction between PERK and ERO1α upon ER stress, demonstrating that PERK and ERO1α interact independently of the PERK UPR function (Figures 6B and S6H). Moreover, a similar pattern of interaction was found for Mfn2. To further test the role of the PERK kinase activity, we treated ER stress-exposed PERK WT and KO cells with the integrated stress response inhibitor (ISRIB), which restores protein translation.[55] Although the PERK kinase domain was irrelevant for the PERK-ERO1α complex, ISRIB partially compromised ER stress-associated MERC strengthening (Figure 6D) and cellular ATP content (Figure 6E). However, ISRIB incubation no longer allowed the decreases in cytoplasmic and mitochondrial ROS that we usually saw under these conditions (Figures 6F and 6G). Therefore, the integrated stress response seems not primarily responsible for the metabolic changes that occur during short-term ER stress but contributes to the altered redox poise during early ER stress.

ERO1α is known for its disulfide bonds within its 3D structure, leading to OX1 and OX2 forms but also to mixed disulfides with its substrates.[31] We used a non-reducing co-immunoprecipitation protocol to test whether ERO1α also forms such mixed disulfides with PERK in HEK293 cells. Indeed, under ER stress conditions, we detected a covalent complex between PERK and ERO1α at a molecular weight of more than 250 kDa (OX4, Figure 7A). A previously characterized ERO1α disulfide-bonded complex migrated just below monomeric PERK at around 150 kDa (OX3, Figure 7A). We therefore sought to identify whether ERO1α used any of its active sites to interact with PERK with four deletion mutants (Δ88-95, Δ96-115, Δ115-155, Δ389-403, Figure S7A). Only the deletion of the C-terminal active site, Δ389-403, fully disrupted the ER stress-dependent interaction (Figure S7A). This raised the possibility that PERK also uses cysteine(s) to interact with ERO1α. In addition to luminal cysteines, we took advantage of a previously described oxidation map of PERK that listed 10 out of 15 cysteines as subject to oxidation.[56] This led to a list of 11 candidate cysteines (asterisk, Figure 7C). Using these point mutants, we determined that a C216 mutation, located within a conserved surface-exposed domain (Figures 7B and S7B), disrupts the increased interaction with ERO1α upon ER stress (Figure S7C). Since C216 is luminal, we tested its mutant for the formation of mixed disulfides with ERO1α upon ER stress. Consistent with our hypothesis, this mutant did not show such complexes (Figure 7A).

Figure 5. PERK-ERO1α modulates ER bioenergetics and redox poise

All data are presented as mean ± standard error of the mean.

(A) ER ATP during tunicamycin treatment. Diagram and movie stills from ERAT4.01 probes. Scale bars: 20 μm.

(B) Average curve profiles from PERK WT and KO MEFs.

(C) Basal ERAT4.01 signals and their drop from tunicamycin treated or not with EN460 (n = 30–68 cells in n = 3 biological replicates per condition, $^{*}p < 0.05$, $^{**}p < 0.01$; $^{****}p < 0.0001$ compared with control; Fisher multiple comparison following one-way ANOVA).

(D–F) Redox state inside the ER during ER stress induction as in Figure 5C. (D) Diagram and movie stills. Scale bars: 20 μm. (E) Control and representative experiment (right). (F) Average of the ER-roGFP2 ratiometric curve profiles. n = 72–158 cells in n = 3–4 biological replicates per condition, \$ or #p < 0.05; \$\$\$\$ or ####p < 0.0001 for WT (\$) or KO (#) Tukey multiple comparison following one-way ANOVA; and $^{*}p < 0.05$; $^{****}p < 0.0001$; Tukey multiple comparison between WT and KO following two-way ANOVA.

(G) Cytoplasmic ROS. Images and signal quantification. Scale bars: 20 μm. Histograms quantifying CellROX signal. n = 9–12 biological replicates for each group, \$\$\$\$ or ####p < 0.0001 for WT (\$) or KO (#) Bonferroni multiple comparison following one-way ANOVA; and $^{**}p < 0.01$; $^{***}p < 0.001$; Bonferroni multiple comparison between WT and KO following two-way ANOVA.

(H) OMM OMM-HyPer/SypHer signals during ER stress induction as in Figure 5C. Amounts are expressed relative to tunicamycin after 1 h (n = 89–204 cells in n = 6–8 biological replicates per condition, $^{*}p < 0.05$; Dunn's multiple comparison between WT and KO following Kruskal-Wallis).

(I) L-lactate measurements as in Figure 5C. (Left) Setup and staining for iLACCO1.2. (Right) iLACCO1.2 signals were normalized as percentage relative to the starting signal. n = 42–98 cells in n = 4 biological replicates per condition, \$\$ or ##p < 0.01; \$\$\$ or ###p < 0.001 respectively compared with WT (\$) or KO (#) DMSO; Bonferroni multiple comparison following one-way ANOVA.

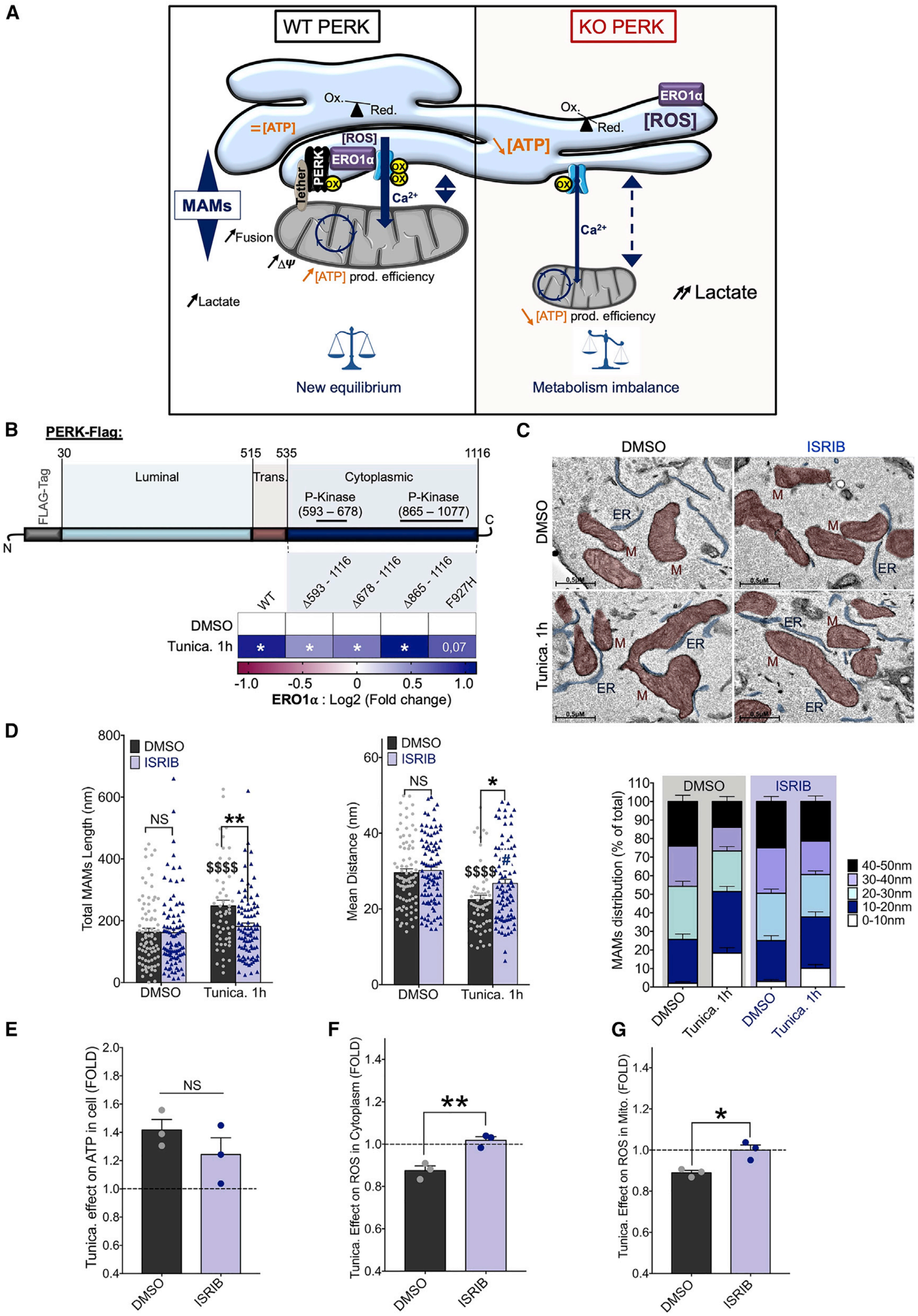

(legend on next page)

To investigate the significance of the PERK-ERO1α complex, we generated PERK rescue stable transfectants within the PERK KO MEF background for WT and C216S mutant PERK. As expected, C216S did not show oligomerized PERK (Figure 7D). Moreover, consistent with these results and the MERC-associated function we described for PERK in Figures 1–6, these mutant rescue cells partially alter the expected MERC remodeling that we were able to recreate with WT PERK rescue (Figure 7E). Moreover, they showed neither decreased cytoplasmic ROS (Figure 7F), nor the typical increased Ca^{2+} release (Figure 7G) upon ER stress. This compromised activity to alter MERCs also did not allow for a rise of the mitochondrial membrane potential (Figure 7H) as well as of cellular bioenergetics (Figure 7I). Therefore, C216 on PERK interacts with the ERO1α triple cysteine active site formed by C391, 394, and 397 to modulate metabolism upon ER stress.

DISCUSSION

Our results identify a mechanism that transmits ER stress on MERCs to adapt mitochondrial bioenergetics. Upon ER stress, following a shock to the metabolic system, the PERK-ERO1α complex restores mitochondrial homeostasis. This restoration is accompanied by increased MERC targeting of the tethers Grp75 and Mfn2, as well as of ER redox enzymes. Among these, the PERK-ERO1α complex forms very specifically, as demonstrated by unbiased MS analysis. Once MERCs have tightened, the PERK-ERO1α complex *decreases* ER Ca^{2+} content and facilitates ER-mitochondria Ca^{2+} transfer to increase mitochondrial fitness. This function of the PERK-ERO1α complex demonstrates in different ways that the time point we were analyzing is not coinciding with pre-apoptosis and is instead reminiscent of the reduction of ER Ca^{2+} signaling toward mitochondria by anti-apoptotic Bcl2.[57] Unlike in the case of calnexin, which increases NOX4-derived ROS in the cytoplasm to oxidize SERCA pumps and *increase* ER Ca^{2+} content, the formation of the PERK-ERO1α complex slightly *reduces* mitochondrial ROS (Figures 5H, S6B, and 6G) in parallel with a slight reduction of the ER oxidative poise (Figures 5E and 5F). In parallel, this maintains mitochondrial Ca^{2+} bioenergetics, accompanied by reduced oxygen consumption and increased membrane potential. Thus, the PERK-ERO1α complex maintains ER bioenergetics and likely prevents cell death during the first minutes of ER stress.

At the ER, formation of the PERK-ERO1α complex triggers oxidation of a variety of MERC proteins, including PERK itself (Figures 2A and 4B). Normally, Prx4 and the glutathione peroxidases GPx7 and GPx8 scavenge ERO1-derived H_2O_2.[30,31] While we were not able to detect interaction of PERK with GPx7 and GPx8, we detected interaction with Prx4, albeit later than with ERO1α (Figure 1E). Thus, ERO1α could be temporarily disconnected from its ROS scavengers before covalently binding to PERK. Moreover, PERK could compete with PDI for ERO1α and disrupt the normal interaction of PDI and ERO1α required to generate ROS.[58] While PDI is known to activate the UPR function of PERK,[59] our findings indicate a UPR-unrelated function of PERK oxidation. In the absence of PERK, ERO1 cannot protect mitochondrial homeostasis, disrupting IP_3Rs oxidation and compromises mitochondrial redox homeostasis.

Our observations raise questions about the relative individual contribution of PERK and ERO1α for mitochondrial and glycolytic metabolism. In our data, we only detected a mild intracellular increase in L-lactate levels after 1 h of tunicamycin-induced ER stress (Figure 5I). In contrast, in the absence of the PERK-ERO1α complex, a glycolysis-related accumulation of L-lactate was detected in the medium in an ERO1-dependent manner (Figure S6F). This suggests that cells evade an energy crisis through the induction of glycolysis if the PERK-ERO1α cannot form. Thus, the metabolic role of ERO1α is dependent on PERK oxidation.

The PERK-ERO1α complex profoundly alters ER-mitochondria Ca^{2+} flux. This flux temporarily increases (Figure 4H) but then decreases to reach a new equilibrium accompanied by increased responsiveness to ER Ca^{2+} release (Figures 4E and 4F). These changes are based on changes of SERCA and IP_3 R-mediated Ca^{2+} handling during ER stress. Potentially, they could also depend on translocon-mediated Ca^{2+} signaling[60] or increased efflux from mitochondria during ER stress. Since the PERK-ERO1α complex increases the mitochondrial membrane potential (Figure 4I), an increased activity of the mitochondrial Na^+/Ca^{2+} exchanger (NCX) in the presence of ROS is more likely.[61] In this scenario, mitochondria would avoid Ca^{2+} overload, which otherwise triggers apoptosis.[62,63] Potentially, such death-promoting functions could be connected to Ire1-mediated MERC signaling, but this role of Ire1 during ER stress has not been investigated.[36] Interestingly, Ire1 itself has also been identified as a redox-sensitive protein, although the significance of this finding for MERCs is currently unknown.[64]

Figure 6. The PERK kinase domain does not interact with ERO1α

All data are presented as mean ± standard error of the mean.

(A) Model.

(B) (Top) Diagram of PERK phospho-kinase domains. (Bottom) Quantification from HEK293 cells treated as in Figure 1A (heatmap, right; n = 3–13 biological replicates, $*p < 0.05$, unpaired t test).

(C) Representative EM images of WT PERK MEFs treated as in Figure 1A in addition to 100 nM ISRIB or DMSO. Scale bar: 500 nm.

(D) EM from ISRIB-treated cells. Mean MERC length (left), distance (middle), and distance distribution (right, as indicated). n = 56–82 MERC analyzed for PERK WT DMSO/1 h tunicamycin pretreated with DMSO; n = 90–95 MERC analyzed for PERK WT DMSO/1 h tunicamycin pretreated with ISRIB in n = 3 technical replicates; \$ or #$p < 0.05$; \$\$\$\$ or ####$p < 0.0001$ compared with DMSO (\$) or tunicamycin (#); Bonferroni multiple comparison following two-way ANOVA; and $*p < 0.05$; $**p < 0.01$ Bonferroni multiple comparison between DMSO and ISRIB pretreatments following two-way ANOVA.

(E) ISRIB blocks improved bioenergetics. Total cellular ATP content per μg of protein determined by luciferase signal.

(F and G) ISRIB prevents oxidative protection of the cytosol and mitochondria. CellROX (F) and MitoSOX (G) signals from cells treated as in Figure 6D were normalized relative to PERK WT and expressed in fold relative to the effect of tunicamycin after 1 h of treatment (n = 3 biological replicates per condition, $*p < 0.05$ or $**p < 0.01$ unpaired t test).

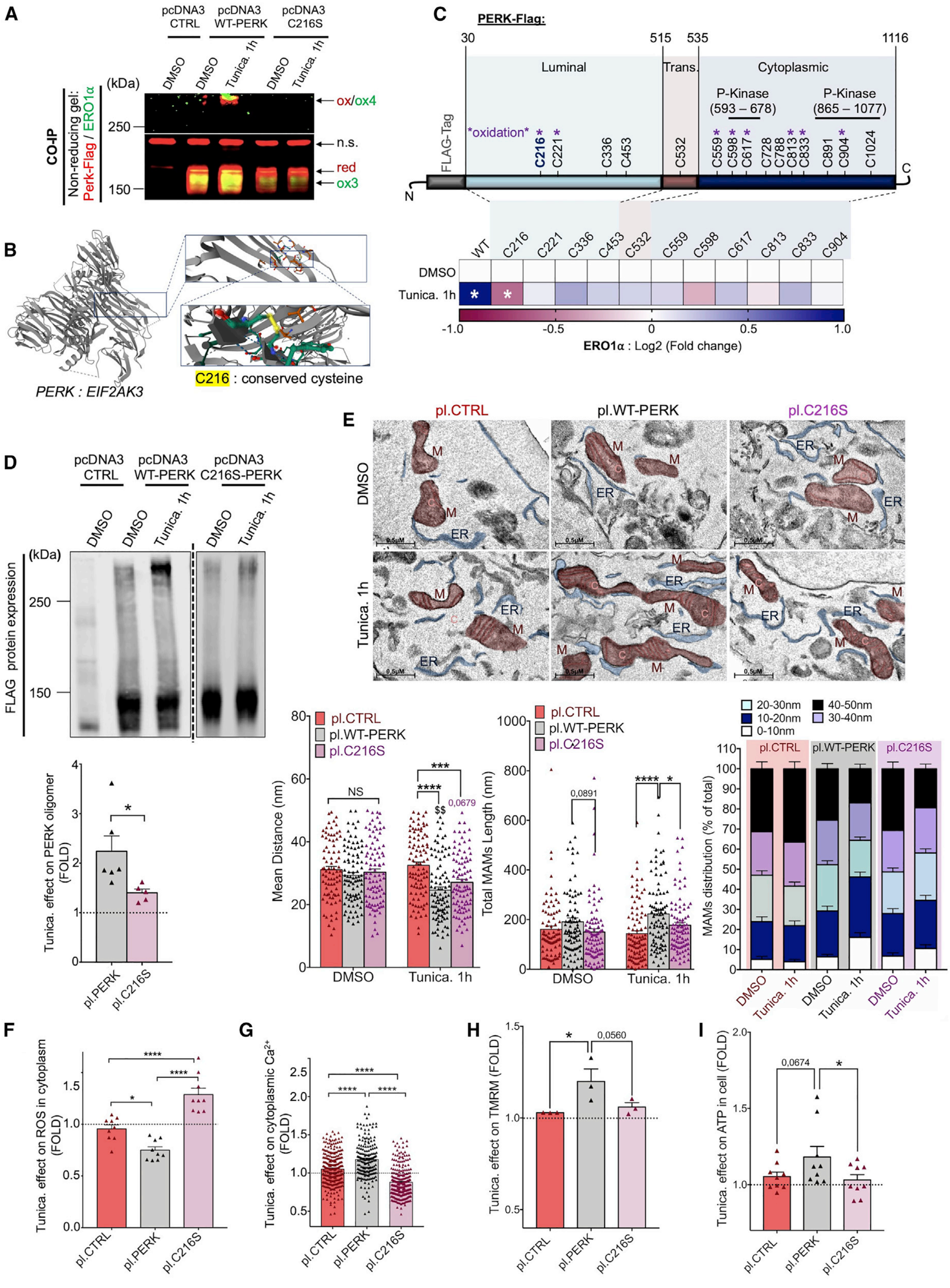

(legend on next page)

For the interaction with ERO1α, PERK uses cysteine 216 and forms a covalent bond with the C-terminal active site of ERO1α. Upon mutation of either site, formation of the covalent complex between PERK and ERO1α is abolished. This shows a redox-based operation of PERK and identifies an additional function of the ERO1α C-terminal active site. Unlike the PERK kinase activity and the ERO1α N-terminal active site, these redox-sensitive sites focus on the restoration of mitochondrial metabolism during the UPR. Solely ER stress-triggered changes in the cellular redox poise appear connected to the integrated stress response function of PERK. This effect may be based on the muted induction of the integrated stress response upon ERO1 inhibition (Figure S2F). Consistent with this hypothesis, PERK inactivated in its kinase domain is still able to interact with ERO1α. PERK contains two additional, cytoplasmic cysteines (C598 and C813), which contribute to the formation of a complex with ERO1α (Figure 7C). These could accommodate additional oxidation within the cytoplasmic domain of PERK.[56] Similar regulatory oxidation occurs for instance on SERCA, where such a modification can turn on or off Ca^{2+} pumping.[65] In the case of PERK, these cytosolic cysteines could control localization to MERCs or PERK dimerization, which could then affect ERO1 interaction. These possibilities remain to be tested.

A prominent effect of the PERK-ERO1α complex is the alteration of MERC architecture and mitochondrial dynamics. While the former is a well-characterized hallmark of ER stress reported by many labs,[5,66] the latter is less well understood. ER stress has been associated with the fusion of mitochondria as a protective response dependent on translational attenuation[67] or under starvation conditions, where it protects from cell death.[68] Our results now suggest these effects may be controlled by the PERK-ERO1α complex, because, in addition to PERK KO, they also depend on ERO1 (Figure S3C and S3D). Another remarkable property of our ER stress conditions are the changes in lipid homeostasis dependent on PERK and ERO1 (Figures S3E–S3H). These changes suggest that MERCs formed during early ER stress not only influence Ca^{2+} and ROS flux but also manipulate lipids in a ROS-dependent manner.

The description of the real-time changes of glycolysis using genetically encoded cytosolic iLACCO1.2 shows that early ER stress immediately increases cytoplasmic L-lactate (Figure 5I). However, these early changes do not depend on the PERK-ERO1α complex. Rather, such changes are only detected upon longer incubation under ER stress, where ERO1 contributes to L-lactate abundance in the culture medium. Thus, the PERK-ERO1α complex could prevent the inefficient use of glucose to generate energy needed for protein folding. This is nicely demonstrated with the drop in ER ATP upon early ER stress when the complex cannot form. To conclude, the PERK-ERO1α complex emerges as a highly responsive adaptive regulator of mitochondria bioenergetics that requires disulfide bonding between its partners to control MERC protein oxidation and Ca^{2+} flux.

Limitations of the study

Our study currently does not identify ER stress as the exclusive trigger of the PERK-ERO1α complex, since its formation did not occur upon dithiothreitol (DTT) treatment but was found with diamide. However, as used in our study, 10 mM DTT likely has effects that go much beyond ER stress and diamide treatment could artificially act as a sort of crosslinker. Titrations of these compounds could address these issues. Moreover, we do not address how ERO1-derived ROS can specifically oxidize MERC proteins. An important caveat is therefore that we are not able to tell whether ERO1 must bind to PERK for this activity, whether it occurs before binding or whether it depends on the enzymatic activity of another protein. Another open question is the role of the cytoplasmic cysteines that are critical for the

Figure 7. PERK cysteine 216 is required for the PERK-ERO1α complex

All data are presented as mean ± standard error of the mean.

(A) Covalent ERO1α/PERK-FLAG complex. HEK293 cells transiently expressing FLAG-tagged WT and PERK-C216S were treated with tunicamycin (10 μg/mL) for 1 h and lysed in the presence of N-ethyl maleimide (NEM). Covalent immunoprecipitated complexes (top) are indicated by overlap of FLAG (red) and ERO1α (green) (n = 1 biological replicate).

(B) Position of PERK-C216S as per Alphafold.

(C) (Top) Diagram of PERK. (Bottom) Quantification of mutant PERK-FLAG immunoprecipitation. HEK293 treated as in Figure 1A were analyzed for co-immunoprecipitating ERO1α (heatmap, right; n = 3–13 biological replicates, *$p < 0.05$, unpaired t test).

(D) PERK oligomers in HEK293 cells expressing CTRL/WT and PERK-C216S as in Figure 2G. Quantification of FLAG dimers (right) (n = 5–6 biological replicates per condition; *$p < 0.05$ Dunn's multiple comparison between WT and PERK-C216S following Kruskal-Wallis).

(E) (Top) PERK-C216S prevents MERC remodeling upon ER stress. EM images of KO PERK MEFs expressing control/WT and PERK-C216S as in Figure 1A. Scale bar: 500 nm. (Bottom) EM quantifications. Mean MERC length (left), MERC distance (middle), and MERC distance distribution as indicated. n = 82–95 MERC analyzed for control DMSO/1 h tunicamycin; n = 91–94 MERC analyzed for WT DMSO/1 h tunicamycin; n = 93–93 MERC analyzed for PERK-C216S DMSO/1 h tunicamycin in n = 3 technical replicates; \$\$, ##$p < 0.01$; compared with control (£)/WT (\$) and C216S (#) under DMSO conditions; Bonferroni multiple comparison following two-way ANOVA; and *$p < 0.05$; **$p < 0.01$ Bonferroni multiple comparison between control/WT and PERK-C216S following two-way ANOVA.

(F) PERK-C216S does not protect the cytosol from ER stress. PERK KO MEFs and WT/PERK-C216S stable rescue transfectants were treated as in Figure 5G (n = 9 biological replicates for each group, *$p < 0.05$ and ****$p < 0.0001$ Dunnett's multiple comparison between PERK KO MEFs and WT/PERK-C216S stable rescue transfectants following one-way ANOVA).

(G) PERK-C216S does not increase cytosolic Ca^{2+} flux upon ER stress. PERK KO MEFs and WT/PERK-C216S stable rescue transfectants were processed and quantified as in Figure S4C and S4D. Signals were normalized relative to the average of signal in the first seconds without ATP and expressed in fold relative to the effect of tunicamycin (n = 182–263 cells in n = 2 biological replicates per condition; ***$p < 0.001$ and ****$p < 0.0001$ Bonferroni multiple comparison between KO expressing PERK-WT and expressing PERK-C216S following one-way ANOVA).

(H and I) PERK-C216S does not modulate mitochondria metabolism upon ER stress. TMRM (H) and total cellular ATP content per microgram of protein (I) were normalized relative to PERK WT (n = 3 biological replicates per condition, Fisher multiple comparison between KO expressing control, PERK-WT, and PERK-C216S following one-way ANOVA).

formation of the PERK-ERO1α complex, for which we could identify Wolcott-Rallison syndrome mutants, in addition to mutations in the proximity of C216. Our experiments do not address how these cytosolic residues influence the mechanism described in this paper. Last, although ERO1 inhibition completely blocks metabolic adaptation upon ER stress, our results have also identified a minor contribution of the integrated stress response for MERC remodeling and bioenergetics.

STAR★METHODS

Detailed methods are provided in the online version of this paper and include the following:

- KEY RESOURCES TABLE
- RESOURCE AVAILABILITY
  - Lead contact
  - Materials availability
  - Data and code availability
- EXPERIMENTAL MODEL AND SUBJECT DETAILS
  - Cell culture
- METHOD DETAILS
  - Generation of new plasmids
  - Protein overexpression
  - Gene silencing
  - Incubation with chemicals
  - pH of the medium
  - Lactate measurement in the medium
  - Mitochondrial activity
  - Total cellular ATP content
  - Flow cytometry
  - Lipid measurements
  - Transmission electronic microscopy
  - Immunofluorescence microscopy
  - Live cell measurements
  - Western blot
  - Co-immunoprecipitation
  - Mass spectrometry
  - Protein redox state
  - Subcellular fractionation
  - Heavy and light membrane fractionation
- QUANTIFICATION AND STATISTICAL ANALYSIS

SUPPLEMENTAL INFORMATION

Supplemental information can be found online at https://doi.org/10.1016/j.celrep.2022.111899.

ACKNOWLEDGMENTS

We thank Bruce Morgan and Paul LaPointe for many helpful suggestions. We thank Richard Wojcikiewicz for the HA-IP3R1 expression construct and Ulla Petäjä-Repo for the myc-SERCA2b expression construct. We thank the following colleagues for critical reagents: Tito Cali for the SPLICS constructs, David Ron for the ER-targeted roGFP2, Roland Malli for the ER-ATP sensor, and Jennifer Rieusset for FATE-1. iLACCO1.2 is subject of a BioRxiv manuscript. We are indebted to Xuejun Sun and the Cell Imaging Facility at the Cross Cancer Institute/University of Alberta for assistance with microscopy. Funding for this study has been provided by CIHR operating grant PS162449 and CRS grant 834492 to T.S., DFG SFB1190 and DFG SFB1027 to I.B., and JSPS KAKENHI 19H05633 to R.E.C.

AUTHOR CONTRIBUTIONS

Conceptualization, T.S. and AB; data curation, A.B., J.C., K.T.-Y., M.C.Y., C.S.G., J.M., T.G., H.M., and A.M.; formal analysis, T.S., I.B., and A.B.; funding acquisition, T.S.; investigation, T.S. and A.B.; methodology, T.S. and A.B.; project administration, T..S; resources, G.N.T.L., S.H., Y.N., R.B., K.B., R.S., E.Z., H.L., and R.E.C.; software, A.B.; supervision, I.B., H.L., R.E.C., and T.S.; validation, T.S. and A.B.; visualization, A.B.; roles/writing – original draft, T.S.; writing – review and editing, T.S., L.M., and A.B.

DECLARATION OF INTERESTS

The authors declare no competing interests.

Received: April 6, 2022
Revised: October 4, 2022
Accepted: December 8, 2022

REFERENCES

1. Braakman, I., and Hebert, D.N. (2013). Protein folding in the endoplasmic reticulum. Cold Spring Harbor Perspect. Biol. *5*, a013201.
2. Princiotta, M.F., Finzi, D., Qian, S.B., Gibbs, J., Schuchmann, S., Buttgereit, F., Bennink, J.R., and Yewdell, J.W. (2003). Quantitating protein synthesis, degradation, and endogenous antigen processing. Immunity *18*, 343–354.
3. Depaoli, M.R., Hay, J.C., Graier, W.F., and Malli, R. (2019). The enigmatic ATP supply of the endoplasmic reticulum. Biol. Rev. Camb. Phil. Soc. *94*, 610–628.
4. Yong, J., Bischof, H., Burgstaller, S., Siirin, M., Murphy, A., Malli, R., and Kaufman, R.J. (2019). Mitochondria Supply ATP to the ER through a Mechanism Antagonized by Cytosolic Ca(2), *8* (Elife).
5. Bravo, R., Vicencio, J.M., Parra, V., Troncoso, R., Munoz, J.P., Bui, M., Quiroga, C., Rodriguez, A.E., Verdejo, H.E., Ferreira, J., et al. (2011). Increased ER-mitochondrial coupling promotes mitochondrial respiration and bioenergetics during early phases of ER stress. J. Cell Sci. *124* (*Pt 13*), 2143–2152.
6. Bernhard, W., and Rouiller, C. (1956). Close topographical relationship between mitochondria and ergastoplasm of liver cells in a definite phase of cellular activity. J. Biophys. Biochem. Cytol. *2* (*4 Suppl*), 73–78.
7. Raturi, A., and Simmen, T. (2013). Where the endoplasmic reticulum and the mitochondrion tie the knot: the mitochondria-associated membrane (MAM). Biochim. Biophys. Acta *1833*, 213–224.
8. Vance, J.E. (2014). MAM (mitochondria-associated membranes) in mammalian cells: lipids and beyond. Biochim. Biophys. Acta *1841*, 595–609.
9. Vance, J.E. (1990). Phospholipid synthesis in a membrane fraction associated with mitochondria. J. Biol. Chem. *265*, 7248–7256.
10. Vance, J.E. (2020). Inter-organelle membrane contact sites: implications for lipid metabolism. Biol. Direct *15*, 24.
11. Anastasia, I., Ilacqua, N., Raimondi, A., Lemieux, P., Ghandehari-Alavijeh, R., Faure, G., Mekhedov, S.L., Williams, K.J., Caicci, F., Valle, G., et al. (2021). Mitochondria-rough-ER contacts in the liver regulate systemic lipid homeostasis. Cell Rep. *34*, 108873.
12. Rizzuto, R., Pinton, P., Carrington, W., Fay, F.S., Fogarty, K.E., Lifshitz, L.M., Tuft, R.A., and Pozzan, T. (1998). Close contacts with the endoplasmic reticulum as determinants of mitochondrial Ca2+ responses. Science *280*, 1763–1766.
13. Bartok, A., Weaver, D., Golenár, T., Nichtova, Z., Katona, M., Bánsághi, S., Alzayady, K.J., Thomas, V.K., Ando, H., Mikoshiba, K., et al. (2019). IP3 receptor isoforms differently regulate ER-mitochondrial contacts and local calcium transfer. Nat. Commun. *10*, 3726.

14. Szabadkai, G., Bianchi, K., Várnai, P., De Stefani, D., Wieckowski, M.R., Cavagna, D., Nagy, A.I., Balla, T., and Rizzuto, R. (2006). Chaperone-mediated coupling of endoplasmic reticulum and mitochondrial Ca2+ channels. J. Cell Biol. *175*, 901–911.
15. Cárdenas, C., Miller, R.A., Smith, I., Bui, T., Molgó, J., Müller, M., Vais, H., Cheung, K.H., Yang, J., Parker, I., et al. (2010). Essential regulation of cell bioenergetics by constitutive InsP3 receptor Ca2+ transfer to mitochondria. Cell *142*, 270–283.
16. Hayashi, T., and Su, T.P. (2007). Sigma-1 receptor chaperones at the ER-mitochondrion interface regulate Ca(2+) signaling and cell survival. Cell *131*, 596–610.
17. Beretta, M., Santos, C.X., Molenaar, C., Hafstad, A.D., Miller, C.C., Revazian, A., Betteridge, K., Schröder, K., Streckfuß-Bömeke, K., Doroshow, J.H., et al. (2020). Nox4 regulates InsP3 receptor-dependent Ca(2+) release into mitochondria to promote cell survival. EMBO J. *39*, e103530.
18. Booth, D.M., Enyedi, B., Geiszt, M., Várnai, P., and Hajnóczky, G. (2016). Redox nanodomains are induced by and control calcium signaling at the ER-mitochondrial interface. Mol. Cell *63*, 240–248.
19. Booth, D.M., Várnai, P., Joseph, S.K., and Hajnóczky, G. (2021). Oxidative bursts of single mitochondria mediate retrograde signaling toward the ER. Mol. Cell *81*, 3866–3876. e2.
20. Kiviluoto, S., Vervliet, T., Ivanova, H., Decuypere, J.P., De Smedt, H., Missiaen, L., Bultynck, G., and Parys, J.B. (2013). Regulation of inositol 1, 4, 5-trisphosphate receptors during endoplasmic reticulum stress. Biochim. Biophys. Acta *1833*, 1612–1624.
21. Bestetti, S., Galli, M., Sorrentino, I., Pinton, P., Rimessi, A., Sitia, R., and Medraño-Fernandez, I. (2020). Human aquaporin-11 guarantees efficient transport of H2O2 across the endoplasmic reticulum membrane. Redox Biol. *28*, 101326.
22. Sorrentino, I., Galli, M., Medraño-Fernandez, I., and Sitia, R. (2022). Transfer of H2O2 from mitochondria to the endoplasmic reticulum via aquaporin-11. Redox Biol. *55*, 102410.
23. Gottschalk, B., Koshenov, Z., Bachkoenig, O.A., Rost, R., Malli, R., and Graier, W.F. (2022). MFN2 mediates ER-mitochondrial coupling during ER stress through specialized stable contact sites. Front. Cell Dev. Biol. *10*, 918691.
24. Hoseki, J., Oishi, A., Fujimura, T., and Sakai, Y. (2016). Development of a stable ERroGFP variant suitable for monitoring redox dynamics in the ER. Biosci. Rep. *36*, e00316.
25. Higo, T., Hattori, M., Nakamura, T., Natsume, T., Michikawa, T., and Mikoshiba, K. (2005). Subtype-specific and ER lumenal environment-dependent regulation of inositol 1, 4, 5-trisphosphate receptor type 1 by ERp44. Cell *120*, 85–98.
26. Ramming, T., Kanemura, S., Okumura, M., Inaba, K., and Appenzeller-Herzog, C. (2016). Cysteines 208 and 241 in Ero1alpha are required for maximal catalytic turnover. Redox Biol. *7*, 14–20.
27. Elgass, K.D., Smith, E.A., LeGros, M.A., Larabell, C.A., and Ryan, M.T. (2015). Analysis of ER-mitochondria contacts using correlative fluorescence microscopy and soft X-ray tomography of mammalian cells. J. Cell Sci. *128*, 2795–2804.
28. Gilady, S.Y., Bui, M., Lynes, E.M., Benson, M.D., Watts, R., Vance, J.E., and Simmen, T. (2010). Ero1alpha requires oxidizing and normoxic conditions to localize to the mitochondria-associated membrane (MAM). Cell Stress Chaperones *15*, 619–629.
29. Anelli, T., Bergamelli, L., Margittai, E., Rimessi, A., Fagioli, C., Malgaroli, A., Pinton, P., Ripamonti, M., Rizzuto, R., and Sitia, R. (2011). Ero1alpha Regulates Ca2+ Fluxes at the Endoplasmic Reticulum-Mitochondria Interface (MAM) (Antioxid Redox Signal).
30. Ramming, T., and Appenzeller-Herzog, C. (2013). Destroy and exploit: catalyzed removal of hydroperoxides from the endoplasmic reticulum. Int. J. Cell Biol. *2013*, 180906.
31. Zito, E., Melo, E.P., Yang, Y., Wahlander, Å., Neubert, T.A., and Ron, D. (2010). Oxidative protein folding by an endoplasmic reticulum-localized peroxiredoxin. Mol. Cell *40*, 787–797.
32. Gutiérrez, T., Qi, H., Yap, M.C., Tahbaz, N., Milburn, L.A., Lucchinetti, E., Lou, P.H., Zaugg, M., LaPointe, P.G., Mercier, P., et al. (2020). The ER chaperone calnexin controls mitochondrial positioning and respiration. Sci. Signal. *13*, eaax6660.
33. de Brito, O.M., and Scorrano, L. (2008). Mitofusin 2 tethers endoplasmic reticulum to mitochondria. Nature *456*, 605–610.
34. Gomez-Suaga, P., Paillusson, S., Stoica, R., Noble, W., Hanger, D.P., and Miller, C.C.J. (2017). The ER-mitochondria tethering complex VAPB-PTPIP51 regulates autophagy. Curr. Biol. *27*, 371–385.
35. Stoica, R., De Vos, K.J., Paillusson, S., Mueller, S., Sancho, R.M., Lau, K.F., Vizcay-Barrena, G., Lin, W.L., Xu, Y.F., Lewis, J., et al. (2014). ER-mitochondria associations are regulated by the VAPB-PTPIP51 interaction and are disrupted by ALS/FTD-associated TDP-43. Nat. Commun. *5*, 3996.
36. Carreras-Sureda, A., Jaña, F., Urra, H., Durand, S., Mortenson, D.E., Sagredo, A., Bustos, G., Hazari, Y., Ramos-Fernández, E., Sassano, M.L., et al. (2019). Non-canonical function of IRE1alpha determines mitochondria-associated endoplasmic reticulum composition to control calcium transfer and bioenergetics. Nat. Cell Biol. *21*, 755–767.
37. Muñoz, J.P., Ivanova, S., Sánchez-Wandelmer, J., Martínez-Cristóbal, P., Noguera, E., Sancho, A., Díaz-Ramos, A., Hernández-Alvarez, M.I., Sebastián, D., Mauvezin, C., et al. (2013). Mfn2 modulates the UPR and mitochondrial function via repression of PERK. EMBO J. *32*, 2348–2361.
38. Verfaillie, T., Rubio, N., Garg, A.D., Bultynck, G., Rizzuto, R., Decuypere, J.P., Piette, J., Linehan, C., Gupta, S., Samali, A., and Agostinis, P. (2012). PERK is required at the ER-mitochondrial contact sites to convey apoptosis after ROS-based ER stress. Cell Death Differ. *19*, 1880–1891.
39. van Vliet, A.R., Giordano, F., Gerlo, S., Segura, I., Van Eygen, S., Molenberghs, G., Rocha, S., Houcine, A., Derua, R., Verfaillie, T., et al. (2017). The ER stress sensor PERK coordinates ER-plasma membrane contact site formation through interaction with filamin-A and F-actin remodeling. Mol. Cell *65*, 885–899. e6.
40. Balsa, E., Soustek, M.S., Thomas, A., Cogliati, S., García-Poyatos, C., Martín-García, E., Jedrychowski, M., Gygi, S.P., Enriquez, J.A., and Puigserver, P. (2019). ER and nutrient stress promote assembly of respiratory chain supercomplexes through the PERK-eIF2alpha Axis. Mol. Cell *74*, 877–890. e6.
41. Arruda, A.P., Pers, B.M., Parlakgül, G., Güney, E., Inouye, K., and Hotamisligil, G.S. (2014). Chronic enrichment of hepatic endoplasmic reticulum-mitochondria contact leads to mitochondrial dysfunction in obesity. Nat. Med. *20*, 1427–1435.
42. Birk, J., Ramming, T., Odermatt, A., and Appenzeller-Herzog, C. (2013). Green fluorescent protein-based monitoring of endoplasmic reticulum redox poise. Front. Genet. *4*, 108.
43. Myhill, N., Lynes, E.M., Nanji, J.A., Blagoveshchenskaya, A.D., Fei, H., Carmine Simmen, K., Cooper, T.J., Thomas, G., and Simmen, T. (2008). The subcellular distribution of calnexin is mediated by PACS-2. Mol. Biol. Cell *19*, 2777–2788.
44. Blais, J.D., Chin, K.T., Zito, E., Zhang, Y., Heldman, N., Harding, H.P., Fass, D., Thorpe, C., and Ron, D. (2010). A small molecule inhibitor of endoplasmic reticulum oxidation 1 (ERO1) with selectively reversible thiol reactivity. J. Biol. Chem. *285*, 20993–21003.
45. Cieri, D., Vicario, M., Giacomello, M., Vallese, F., Filadi, R., Wagner, T., Pozzan, T., Pizzo, P., Scorrano, L., Brini, M., and Calì, T. (2018). SPLICS: a split green fluorescent protein-based contact site sensor for narrow and wide heterotypic organelle juxtaposition. Cell Death Differ. *25*, 1131–1145.
46. Calì, T., and Brini, M. (2021). Quantification of organelle contact sites by split-GFP-based contact site sensors (SPLICS) in living cells. Nat. Protoc. *16*, 5287–5308.
47. Doghman-Bouguerra, M., Granatiero, V., Sbiera, S., Sbiera, I., Lacas-Gervais, S., Brau, F., Fassnacht, M., Rizzuto, R., and Lalli, E. (2016). FATE1 antagonizes calcium- and drug-induced apoptosis by uncoupling ER and mitochondria. EMBO Rep. *17*, 1264–1280.

48. Wu, J., Prole, D.L., Shen, Y., Lin, Z., Gnanasekaran, A., Liu, Y., Chen, L., Zhou, H., Chen, S.R.W., Usachev, Y.M., et al. (2014). Red fluorescent genetically encoded Ca2+ indicators for use in mitochondria and endoplasmic reticulum. Biochem. J. *464*, 13–22.

49. Luo, Y., Bond, J.D., and Ingram, V.M. (1997). Compromised mitochondrial function leads to increased cytosolic calcium and to activation of MAP kinases. Proc. Natl. Acad. Sci. USA. *94*, 9705–9710.

50. Brand, M.D., and Nicholls, D.G. (2011). Assessing mitochondrial dysfunction in cells. Biochem. J. *435*, 297–312.

51. Kassenbrock, C.K., and Kelly, R.B. (1989). Interaction of heavy chain binding protein (BiP/GRP78) with adenine nucleotides. EMBO J. *8*, 1461–1467.

52. Samtleben, S., Mina, L., Yap, M.C., Branton, W.G., Yousuf, M.S., Tenorio, G., Ballanyi, K., Giuliani, F., Kerr, B.J., Power, C., and Simmen, T. (2022). Astrocytes Show Increased Levels of Ero1alpha in Multiple Sclerosis (MS) and its Experimental Autoimmune Encephalomyelitis (EAE) Animal Model (Eur J Neurosci).

53. Varone, E., Chernorudskiy, A., Cherubini, A., Cattaneo, A., Bachi, A., Fumagalli, S., Erol, G., Gobbi, M., Lenardo, M.J., Borgese, N., and Zito, E. (2022). ERO1 alpha deficiency impairs angiogenesis by increasing N-glycosylation of a proangiogenic VEGFA. Redox Biol. *56*, 102455.

54. Konno, T., Pinho Melo, E., Lopes, C., Mehmeti, I., Lenzen, S., Ron, D., and Avezov, E. (2015). ERO1-independent production of H2O2 within the endoplasmic reticulum fuels Prdx4-mediated oxidative protein folding. J. Cell Biol. *211*, 253–259.

55. Sidrauski, C., Acosta-Alvear, D., Khoutorsky, A., Vedantham, P., Hearn, B.R., Li, H., Gamache, K., Gallagher, C.M., Ang, K.K.H., Wilson, C., et al. (2013). Pharmacological brake-release of mRNA translation enhances cognitive memory. Elife *2*, e00498.

56. Xiao, H., Jedrychowski, M.P., Schweppe, D.K., Huttlin, E.L., Yu, Q., Heppner, D.E., Li, J., Long, J., Mills, E.L., Szpyt, J., et al. (2020). A quantitative tissue-specific landscape of protein redox regulation during aging. Cell *180*, 968–983. e24.

57. Foyouzi-Youssefi, R., Arnaudeau, S., Borner, C., Kelley, W.L., Tschopp, J., Lew, D.P., Demaurex, N., and Krause, K.H. (2000). Bcl-2 decreases the free Ca2+ concentration within the endoplasmic reticulum. Proc. Natl. Acad. Sci. USA. *97*, 5723–5728.

58. Masui, S., Vavassori, S., Fagioli, C., Sitia, R., and Inaba, K. (2011). Molecular bases of cyclic and specific disulfide interchange between human ERO1alpha protein and protein-disulfide isomerase (PDI). J. Biol. Chem. *286*, 16261–16271.

59. Kranz, P., Neumann, F., Wolf, A., Classen, F., Pompsch, M., Ocklenburg, T., Baumann, J., Janke, K., Baumann, M., Goepelt, K., et al. (2017). PDI is an essential redox-sensitive activator of PERK during the unfolded protein response (UPR). Cell Death Dis. *8*, e2986.

60. Lang, S., Pfeffer, S., Lee, P.H., Cavalié, A., Helms, V., Förster, F., and Zimmermann, R. (2017). An Update on Sec61 channel functions, mechanisms, and related diseases. Front. Physiol. *8*, 887.

61. Wagner, S., Rokita, A.G., Anderson, M.E., and Maier, L.S. (2013). Redox regulation of sodium and calcium handling. Antioxidants Redox Signal. *18*, 1063–1077.

62. Csordás, G., Thomas, A.P., and Hajnóczky, G. (1999). Quasi-synaptic calcium signal transmission between endoplasmic reticulum and mitochondria. EMBO J. *18*, 96–108.

63. Scorrano, L., Oakes, S.A., Opferman, J.T., Cheng, E.H., Sorcinelli, M.D., Pozzan, T., and Korsmeyer, S.J. (2003). BAX and BAK regulation of endoplasmic reticulum Ca2+: a control point for apoptosis. Science *300*, 135–139.

64. Oka, O.B.V., Pierre, A.S., Pringle, M.A., Tungkum, W., Cao, Z., Fleming, B., and Bulleid, N.J. (2022). Activation of the UPR sensor ATF6alpha is regulated by its redox-dependent dimerization and ER retention by ERp18. Proc. Natl. Acad. Sci. USA. *119*. e2122657119.

65. Dremina, E.S., Sharov, V.S., Davies, M.J., and Schöneich, C. (2007). Oxidation and inactivation of SERCA by selective reaction of cysteine residues with amino acid peroxides. Chem. Res. Toxicol. *20*, 1462–1469.

66. Csordás, G., Renken, C., Várnai, P., Walter, L., Weaver, D., Buttle, K.F., Balla, T., Mannella, C.A., and Hajnóczky, G. (2006). Structural and functional features and significance of the physical linkage between ER and mitochondria. J. Cell Biol. *174*, 915–921.

67. Lebeau, J., Saunders, J.M., Moraes, V.W.R., Madhavan, A., Madrazo, N., Anthony, M.C., and Wiseman, R.L. (2018). The PERK arm of the unfolded protein response regulates mitochondrial morphology during acute endoplasmic reticulum stress. Cell Rep. *22*, 2827–2836.

68. Gomes, L.C., Di Benedetto, G., and Scorrano, L. (2011). During autophagy mitochondria elongate, are spared from degradation and sustain cell viability. Nat. Cell Biol. *13*, 589–598.

69. Soulsby, M.D., and Wojcikiewicz, R.J.H. (2007). Calcium mobilization via type III inositol 1, 4, 5-trisphosphate receptors is not altered by PKA-mediated phosphorylation of serines 916, 934, and 1832. Cell Calcium *42*, 261–270.

70. Tuusa, J.T., Leskelä, T.T., and Petäjä-Repo, U.E. (2010). Human delta opioid receptor biogenesis is regulated via interactions with SERCA2b and calnexin. FEBS J. *277*, 2815–2829.

71. Vishnu, N., Jadoon Khan, M., Karsten, F., Groschner, L.N., Waldeck-Weiermair, M., Rost, R., Hallström, S., Imamura, H., Graier, W.F., and Malli, R. (2014). ATP increases within the lumen of the endoplasmic reticulum upon intracellular Ca2+ release. Mol. Biol. Cell *25*, 368–379.

72. Cabibbo, A., Pagani, M., Fabbri, M., Rocchi, M., Farmery, M.R., Bulleid, N.J., and Sitia, R. (2000). ERO1-L, a human protein that favors disulfide bond formation in the endoplasmic reticulum. J. Biol. Chem. *275*, 4827–4833.

73. Raturi, A., Gutiérrez, T., Ortiz-Sandoval, C., Ruangkittisakul, A., Herrera-Cruz, M.S., Rockley, J.P., Gesson, K., Ourdev, D., Lou, P.H., Lucchinetti, E., et al. (2016). TMX1 determines cancer cell metabolism as a thiol-based modulator of ER-mitochondria Ca2+ flux. J. Cell Biol. *214*, 433–444.

74. Folch, J., Lees, M., and Sloane Stanley, G.H. (1957). A simple method for the isolation and purification of total lipides from animal tissues. J. Biol. Chem. *226*, 497–509.

75. Abreu, S., Solgadi, A., and Chaminade, P. (2017). Optimization of normal phase chromatographic conditions for lipid analysis and comparison of associated detection techniques. J. Chromatogr. A *1514*, 54–71.

76. Theurey, P., Tubbs, E., Vial, G., Jacquemetton, J., Bendridi, N., Chauvin, M.A., Alam, M.R., Le Romancer, M., Vidal, H., and Rieusset, J. (2016). Mitochondria-associated endoplasmic reticulum membranes allow adaptation of mitochondrial metabolism to glucose availability in the liver. J. Mol. Cell Biol. *8*, 129–143.

77. Koopman, W.J.H., Visch, H.J., Verkaart, S., van den Heuvel, L.W.P.J., Smeitink, J.A.M., and Willems, P.H.G.M. (2005). Mitochondrial network complexity and pathological decrease in complex I activity are tightly correlated in isolated human complex I deficiency. Am. J. Physiol. Cell Physiol. *289*, C881–C890.

78. Cieri, D., Vicario, M., Giacomello, M., Vallese, F., Filadi, R., Wagner, T., Pozzan, T., Pizzo, P., Scorrano, L., Brini, M., and Cali, T. (2017). SPLICS: A Split Green Fluorescent Protein-Based Contact Site Sensor for Narrow and Wide Heterotypic Organelle Juxtaposition (Cell Death Differ).

79. Tubbs, E., and Rieusset, J. (2016). Study of endoplasmic reticulum and mitochondria interactions by in situ proximity ligation assay in fixed cells. JoVE *118*, 54899.

80. Tubbs, E., Theurey, P., Vial, G., Bendridi, N., Bravard, A., Chauvin, M.A., Ji-Cao, J., Zoulim, F., Bartosch, B., Ovize, M., et al. (2014). Mitochondria-associated endoplasmic reticulum membrane (MAM) integrity is required for insulin signaling and is implicated in hepatic insulin resistance. Diabetes *63*, 3279–3294.

81. Shen, Y., Rosendale, M., Campbell, R.E., and Perrais, D. (2014). pHuji, a pH-sensitive red fluorescent protein for imaging of exo- and endocytosis. J. Cell Biol. *207*, 419–432.

82. Zhang, X., Gibhardt, C.S., Will, T., Stanisz, H., Körbel, C., Mitkovski, M., Stejerean, I., Cappello, S., Pacheu-Grau, D., Dudek, J., et al. (2019). Redox signals at the ER-mitochondria interface control melanoma progression. EMBO J. *38*, e100871.

83. Trahan, C., Aguilar, L.C., and Oeffinger, M. (2016). Single-step affinity purification (ssAP) and mass spectrometry of macromolecular complexes in the yeast S. cerevisiae. Methods Mol. Biol. *1361*, 265–287.

84. Wieckowski, M.R., Giorgi, C., Lebiedzinska, M., Duszynski, J., and Pinton, P. (2009). Isolation of mitochondria-associated membranes and mitochondria from animal tissues and cells. Nat. Protoc. *4*, 1582–1590.

STAR★METHODS

KEY RESOURCES TABLE

REAGENT or RESOURCE	SOURCE	IDENTIFIER
Antibodies		
Biotin	Sigma-Aldrich	Cat# B3640, RRID:AB_258552
IP3R1	Thermo-Fisher	PA1-901
IP3R1	Millipore	#3809289
MCU	Sigma-Aldrich	HPA-016480
ATF6	Abcam	Cat# ab203119, RRID:AB_2650448
c-Myc	Cell-Signaling	D84C12 Cat# 5605, RRID:AB_1903938
c-Myc 9E10	Invitrogen	13-2500
CHOP	Invitrogen	MAA250
Drp1	Cell-Signaling	D6C7 Cat# 8570, RRID:AB_10950498
eif2-α	Cell-Signaling	9722
ERO1-α	Millipore	MABT376
ERO1-α	Gene Tex	GTX112589 Cat# GTX112589, RRID:AB_2036877
ERO1-β	Abcam	197290
ERO1-β	Invitrogen	PA-5-25-142
FACL4	Abcam	Cat# ab110007, RRID:AB_10864423
Flag-Tag	Cell-Signaling	D6W5B
Flag-Tag	Sigma-Aldrich	F7425
GPx7	Invitrogen	2704.
GPx8	Abcam	183664
Grp78 (BIP)	BD Transduction	610979
HA-Tag	Cell-Signaling	C29F4
Idh2	Proteintech.	Cat# 15932-1-AP, RRID:AB_2264612
Ire1	Cell-Signaling	14C10 Cat# 3294, RRID:AB_823545
Mfn2	Abcam	205236
mtHsp70 (Grp75)	Thermo-Scientific	MA3-028
Myc	Invitrogen	9.E10
NOX4	Invitrogen	PA5-76073
NOX4	Abcam	Cat# ab109225, RRID:AB_10861375
PDI	Invitrogen	MA3-019
PERK	Abcam	Cat# ab65142, RRID:AB_1142220
PERK (human)	R&D	AF3999
Phospho (Ser.724)-Ire1	Abcam	Cat# ab48187, RRID:AB_873899
Phospho (Ser51)-eif2-α	Cell-Signaling	119A11
Phospho (Tyr.980)-Perk	Cell-Signaling	16F8
PRDX4	Abcam	184167
SERCA2	Millipore	MAB-2636
VDAC1	Abcam	Cat# ab14734, RRID:AB_443084
VDAC1	B.D. Bioscience	478
VDAC1	Aviva System Biology	Cat# ARP35122_T100, RRID:AB_842641
XBP1 (unsplice and splice form)	Abcam	Cat# ab37152, RRID:AB_778939
γ-Tubulin	Thermo-Scientific	MA1-850
anti-Mouse	Invitrogen	A21057
anti-Rabbit	Invitrogen	A11369

(*Continued on next page*)

Continued

REAGENT or RESOURCE	SOURCE	IDENTIFIER
anti-Goat	Invitrogen	A21084
488 (Green) anti-IgG-Mouse	Invitrogen AlexaFluor	A11029
488 (Green) anti-IgG-Rabbit	Invitrogen AlexaFluor	A11034
405 (Blue) anti-IgG-Mouse	Life technology AlexaFluor	A31553
405 (Blue) anti-IgG-Rabbit	Life technology AlexaFluor	A31556
594 (Red) anti-IgG-Mouse	Invitrogen AlexaFluor	A11005
594 (Red) anti-IgG-Rabbit	Invitrogen AlexaFluor	A11012
405 (Blue) anti-IgG1-Mouse	Dylight^{TM}	409109
488 (Green) anti-IgG2a-Mouse	Invitrogen AlexaFluor	A21131
Bacterial and virus strains		
DH5α	Thermo-Scientific	18265017
Chemicals, peptides, and recombinant proteins		
2-β-Mercaptoethanol	Sigma-Aldrich	M3148
Acetone	Fisher Cl	A18-1
Acrylamide	BioRad	1610158
AMG’44	Tocris	5517
Annexin V-FITC apoptosis kit	BD Pharmingen^{TM}	556547
Annexin-V-Cy3 kit	Biovision	K102-100
Anti-Flag(R) M2 Magnetics Beads	Sigma-Aldrich	M8823
APS (Amonium Persulfate)	BioRad	1610700
ATP	Sigma-Aldrich	A2383
ATP Kit Detection	Invitrogen Molecular Probes	A22066
BAPTA-AM	Sigma-Aldrich	B6769
BCA kit	Pierce^{TM} Thermo Scientific	23225
BFA (Brefeldin A)	Alexis Biochemicals	350 - 019- M010
BIAM(Iodoacetyl-PEG2-Biotin) E2-link^{TM}	Thermo-Scientific	21334
BSA	Sigma-Aldrich	A9647
BSA free fatty acid	Sigma-Aldrich	A6003
CellROX Green	Invitrogen	C10444
CellROX Orange	Invitrogen	C10493A
CHAPS	Sigma-Aldrich	Sial
Citrate synthase assay kit	Abcam	239712
Coomassie blue P-250	BioRad	161-0436
Complete protease inhibitors (x25)	Roche	11873580001
Cytometer setup and tracking beads	B.D Bioscience	642412
D-Glucose anhydrous	Fluka/Biochemika	49139
D-Luciferin monosodium salt	Pierce^{TM}	88291
D-Luciferin sodium salt	Invitrogen	A22066
D-Mannitol, ACS reagent	Sigma-Aldrich	M9647
Dapi	Sigma-Aldrich	D9542
Diamide	Sigma-Aldrich	D3648
DL-Buthiamine Sulfoximin	Sigma-Aldrich	19176
DMEM (4,5g of Glucose)	Gibco	11995-065
DMSO	Sigma-Aldrich	D2650
DPBS (10x) with Ca^{2+}/Mg^{2+}	Gibco	14200-075
DPBS (10x) without Ca^{2+}/Mg^{2+}	Gibco	14080-055
DSP	Thermo-Scientific	22585
DTT(Dithiothreitol)	Invitrogen	A22066A
DYKDDDDK Synthetic Peptide Elution	SinoBiological	PP101274

(*Continued on next page*)

Continued

REAGENT or RESOURCE	SOURCE	IDENTIFIER
Dynbeads^{TM} ProteinA	Invitrogen	10002D
EDTA	Sigma-Aldrich	E5134
EGTA	OmniPur EMD	4100
EN460	Millipore	328501
FBS	Sigma-Aldrich	F1051
FCCP (Carbonyl cyanide 4-(trifluoromethoxy)phenylhydrazone)	Cayman	15218
FCCP (Carbonyl cyanide 4-(trifluoromethoxy)phenylhydrazone) (for respiration)	Sigma-Aldrich	C2920
Fluo-8L(AM)	AAT Bioquest	21097
Geneticin (G418 sulphate)	Gibco	10131-027
GKT 137831	Cayman	17764
Glass bottom culture dishes	MatTeck	Part. NO. P35-G-1.0-14-C
Glutathione esthyl ester	Cayman Chemical	14953
Glycolysis cell-based assay kit	Cayman	600450
GSK 2606414	Tocris	5107
HBSS (1x) with Ca^{2+} Chloride/Mg^{2+} Chloride/ Mg^{2+} Sulfate	Gibco	14025-092
HBSS (1x) without Ca^{2+} Chloride/Mg^{2+} Chloride/ Mg^{2+} Sulfate	Gibco	14175-095
HEPES	Fisher BioReagents	BP310-500
Histamine	Sigma-Aldrich	H7250
Immersion oil	Zeiss	1111808
IRE-A Inhibitor III	Calbiochem	N/A
Isopropanol (2-Propanol)	Sigma-Aldrich	439207
ISRIB	Sigma-Aldrich	SML0843 (5mg)
Lactate kit	Cayman	600455
Laemmli sample buffer (2x)	BioRad	1610737
Lipofectamine^{TM} 3000	Invitrogen	L3000-015
Metafectene® Pro	Biontex	RKP203 (T040-2.0)
Methanol	Sigma-aldrich	34860-4L-R
$MgCl_2$	EM Science	MX0045-1
$MgSO_4$	Sigma-aldrich	230391
Microscope Cover glass	Fisherbrand^{TM} Fisher Scientific	12-545-82
Microscope Cover glass	Fisherbrand^{TM} Fisher Scientific	12-545-82 / 12CIR #1D
Microscopes slides	Fisherbrand^{TM}	12-552-3
MitoLite^{TM} Blue FX490	Cayman	25159
Mitosox^{TM} RED Mitochondrial	Invitrogen	M36008
Mitotracker CMXROS	Molecular Probes	M7512
MKT 077	TOCRIS	4621 (10mg)
NAC (N-Acetyl-L-cysteine)	Sigma-aldrich	A9165
NEM (N-Ethylmaleimide)	Sigma-aldrich	E-3876
NH_4Cl	Sigma-aldrich	A9434
Nitrocellulose (0,45µM) membranes	BioRad	1620115
Oligofectamine	Invitrogen	12252-011
Oligomycin (for respiration)	Abcam	141829
Oligomycin A	Cayman	15218
Paraformaldehyde (16%)	Electron Microscopy Science (EMS)	15710
PE-Annexin V-Apoptosis dectection kit I	BD Pharmingen^{TM}	559763

(*Continued on next page*)

Continued

REAGENT or RESOURCE	SOURCE	IDENTIFIER
Percoll	GE Healthcare	17-0891-02
Phospho-STOP (x10)	Roche	4693159001
Pluronic F-124	Invitrogen	P3000MP
Poly-L-Lysine	Sigma-Aldrich	P4707
Protein Dual color	BioRad	1610374
Mounting Medium	MJS-Biolynx inc.	VECTH19002 VECTASHIELD® PLUS Antifade
Mounting Medium	Prolong^{TM} Gold antifade reagent	P36934
RNAi ERO1α (20nMol)	Invitrogen	IMS55224898
RNAi negative control	Steath^{TM} Invitrogen	452001
Saponin	Sigma-aldrich	Fluka 47036
TBHQ (Tert-Butylhydroquinone 97%)	Sigma-aldrich	112941
Temed	Sigma-aldrich	T9281
TMRM	Invitrogen	(871370) T668
Triton (x100)	Sigma-aldrich	1086431000
Trypan blue (0,4%)	Gibco	15250-061
Trypsin-EDTA(1x) 0,25%	Gibco	25200-072
Tunicamycin	TOCRIS	3516
Tunicamycin	Sigma-Aldrich	654380
Thapsigargin	Thermo Fisher Scientific, Waltham, MA	N/A
Brefeldin A	Alexis Biochemicals	BFA, 350-019-M010
EN460	Millipore	328501
GKT 137831	Cayman	17764
AMG'44	Tocris	5517
N-acetyl-L-cysteine (NAC)	Sigma-Aldrich	A9165
TBHP	Invitrogen	C10493A
dithiothreitol (DTT)	Invitrogen	A22066A
diamide	Sigma-Aldrich	D3648
DL-buthionine-sulfoximine (BSO)	Sigma-Aldrich	B2640
glutathione ethyl ester (GSH)	Cayman Chemical	14953
oligomycin A	Cayman	15218
BAPTA-AM	Sigma-Aldrich	B6769
ISRIB	Sigma-Aldrich	SML0843
DMSO	Sigma-Aldrich	D2650
BCA Protein Assay Kit	Pierce^{TM} Thermo Scientific	23225
protease inhibitors	Roche	Complete, 11873580001
PLA Mouse Minus	SigmaAldrich	#DU092004
PLA rabbit PLUS	SigmaAldrich	#DUO92002
PLA kit	SigmaAldrich, Duolink®	#DU092008
Deposited data		
Mass spectrometry	https://repository.jpostdb.org/entry/JPST001942	
Experimental models: Cell lines		
PERK KO (sex unknown)	ATCC	CVCL_B067
HeLa (female)	ECACC, Porton Down, UK	CVCL_0030
HEK293 (female)	ECACC, Porton Down, UK	CVCL_0043
ERO1α KO	Mario Negri Institute for Pharmacological Research, Milan, Italy	Dr. Ester Zito's Laboratory

(*Continued on next page*)

Continued

REAGENT or RESOURCE	SOURCE	IDENTIFIER
Oligonucleotides		
RNAi control	Invitrogen	452001
RNAi Ero1α	Invitrogen	IMS55224898
RNAi PERK	Invitrogen	HSS190343 / HSS190344
RNAi transfection reagent	Invitrogen	Oligofectamine$^{\text{TM}}$ 12252-01
Recombinant DNA		
pcDNA IP$_3$R1-HA	Richard J. Wojcikiewicz, Syracuse, USA	Publication[69]
pcDNA SERCA-2B	Ulla Petäjä-Repo, Helsinki, Finland	Publication[70]
pcDNA ERroGFP2	C. Appenzeller-Herzog lab, Basel, Swiss	Publication[42]
pcDNA ERAT4.01	Rolland Malli, Graz, Austria	Publication[71]
pcDNA SPLICS (Long and Short)	Tito Cali lab, Padova, Italy	Publication[45]
pcDNA4-GFP-P2A-FATE1	Jennifer Rieusset, Lyon, France	Publication[47]
iLACCAO1.2	R. Campbell lab, Tokyo, Japan	Submittied in BioRxiv manuscript
All pcDNAs FLAG-PERK	Precision Biolaboratories	This paper
pcDNA ERO1α and mutants thereof	Roberto Sitia, Milan, Italy	Publication[72]
pcDNA ER-GECO, Mito-RGECO	Robert Campbell, Tokyo, Japan	Publication[32,73]
Software and algorithms		
Flow cytometry software	Fortessa	BD FACSDiva
Microscope acquisition and analysis software	Zeis	AxioVision 40 V4.8.0.0
Deconvolution	Huygens Professional	Deconvolution version 20.04 - SVI (Scientific Volume Imaging)
Confocal acquisition and analysis software	Olympus FluoView software	PL-A686 6.6 megapixel camera (Capture SE software, Pixelink) and acquired with Olympus FluoView software camera (Capture SE software, Pixelink)
Other		
FACS	Fortessa	BD LSR
Scanner	Odyssey Licor	Version 1.1
Plate Reader	Bioteck	Synergy 4
Microscope	Zeiss	Zeiss observer Z1 (Inverted Phase Contrast Fluorescence Microscope)
Microscope confocal with a perfusion system consisting of a peristaltic pump	Olympus	V1000 laser- scanning confocal microscope using a 60× objective [XLUMPLANFL, numerical aperture (NA) 1.0; Olympus] or a 20× objective (XLUMPLANFL, NA 1.0; Olympus), equipped with a per- fusion system consisting of a peristaltic pump (for the FV1000 system, Watson-Marlow Alitea-AB; Sin-Can)
Centrifuge	Eppendorf	S415R
Centrifuge	Beckman	J2-21M
UltraCentrifuge / Rotor	Beckman Coulter	Beckman Coulter 25905190TiRotor
Ultracentrifuge /Rotor	Beckman Coulter	Optima$^{\text{TM}}$ -MAX-XP Centrifuge TLA120.2 Rotor
Centrifuge	Eppendorf	5810R, 15 amp Version

(*Continued on next page*)

Continued

REAGENT or RESOURCE	SOURCE	IDENTIFIER
Oxygraph	Oroboros instruments Corp, Austria	Oxygraph 2k (TIP-2k/ Mainboard A-0159) Oroboros O2k
Ultracentrifuge tubes	Beckman Coulter	ref: 361623
Ultracentrifuge Polycarbonate tubes	Beckman Coulter	ref: 343778
Automatic cell counter, Countess II FL	Life Technologies	A27974
Cell Chamber, Hemacytometer	Life Technologies	A25750

RESOURCE AVAILABILITY

Lead contact

Further information and requests for resources and reagents should be directed to and will be fulfilled by the lead contact, Thomas Simmen (Thomas.Simmen@ualberta.ca).

Materials availability

Newly generated plasmids are available upon completion of an MTA with the University of Alberta.

Data and code availability

- Proteomic data have been deposited at https://repository.jpostdb.org/entry/JPST001942 and are publicly available as of the date of publication. The DOI is listed in the key resources table. Full Western blot and microscopy data, as well as any additional information required to reanalyze the data reported in this paper will be shared by the lead contact upon request.
- No original code has been generated.
- Any additional information required to reanalyze the data reported in this paper is available from the lead contact upon request.

EXPERIMENTAL MODEL AND SUBJECT DETAILS

Cell culture

Experiments were conducted on mouse embryogenic fibroblasts (MEFs; PERK-KO were from ATCC), HeLa cells, or human embryonic kidney 293 (HEK293) cells (ECACC, Porton Down, UK). Ero1α-KO MEFs were from Dr. Ester Zito's Laboratory (Mario Negri Institute for Pharmacological Research, Milan, Italy). RRIDs: PERK KO: CVCL_B067*, HeLa:* CVCL*_0030, HEK293:* CVCL*_0043.*

Cells were cultured in Dulbecco's Modified Eagle's Medium (DMEM, PAA Laboratories) containing 25 mM glucose and 10% fetal bovine albumin serum (FBS, F1051, Sigma-Aldrich), at 37°C and in a humid atmosphere with 5% CO$_2$.

METHOD DETAILS

Generation of new plasmids

The FLAG-PERK expressing plasmids were generated by Precision Biolaboratories (Rakesh Bhat, St. Albert, AB) from a synthetic template that introduces an FLAG tag after the signal peptide at amino acid 30 (Geneart, Thermo Fisher) using the Q5 Site-Directed Mutagenesis Kit (NEB) or the Phusion Site-Directed Mutagenesis Kit (Thermo Fisher). The full synthesized sequence is available upon request.

Ero1α-expressing plasmids were generated in the Sitia lab on a previously described template.[72] Deletion mutants were constructed by PCR using the splicing by overlap extension technique. Primer sequences are as follows (with novel restriction sites highlighted): Δ86-95 (PstI), FW: CAGTCTCTT**CTGCAG**GGCCTCTTCAGGTTTACCTTG, Rev: GGCC**CTGCAG**AAGAGACTGTGCTGTCAAACCATG; Δ96-115 (NheI), FW: **GCTAGC**AGATCCACACTGGCTGATGTCATTC, Rev: CCAGTGTGGATCT**GCTAGC**TACAAGTATTCTGAAGAAG; Δ115-155 (PstI), FW: CCA**CTGCAG**AACTTTAATCCCATCAGGAACTTCATCAGATTG, Rev: ATGGGATTAAAGTT**CTGCAG**TGGACCAAGCATGATG; Δ389-403 (BamHI), FW: ACCCTGAGTCT**GGATCC**TTGAAATATTTCTAAAATGCAGTC, Rev: TTTCAA**GGATCC**AGACTCAAGGTTTAGGCACTGCTCTGAAGATCTTAT. The final PCR products were cloned using the pGEM-T-easy cloning kit (Promega, Milan, Italy) and sequenced. The cDNAs were excised with Acc65I and XbaI and inserted in-frame into pcDNA3.1myc/his (–) (Invitrogen).

Protein overexpression

At least 24h after seeding, cells were transfected with plasmids (pcDNA3, pcDNA4, pcDNA5) encoding PERK-Flag, PERK-Flag mutant, Ero1α-MYC, Ero1α-MYC mutants, IP$_3$R1-HA,[69] SERCA2b,[70] SPLICS (Long and Short), Sec61-BFP, ER and mitochondrial

Ca^{2+} indicators (ER-RGECO, Mito-RGECO), a redox poise indicator expressed in ER (ERroGFP2), and ER-ATP indicators (ERAT4.01), a ER-mitochondria spacer (pcDNA4-GFP-P2A-FATE1) and a L-lactate indicator (iLACCAO1.2). Transfection was done using Metafectene® Pro (RKP203 (T040-2.0), Biontex) for HEK 293 cells and Lipofectamine™ 3000 (L3000-015, Invitrogen) for MEFs and HeLa cells following the technical recommendations of the manufacturer. Experiments were performed 24h or 48 h after transfection, with at least 50% of the cells transfected.

Gene silencing

At least 24h after seeding, cells were transfected with control (20–30 nmol/L, 452001, Invitrogen), Ero1α (30 nmol/L, IMS55224898, Invitrogen), or PERK (20–30 nmol/L, HSS190343 and HSS190344, Invitrogen) RNAi using Oligofectamine™ (12252-01, Invitrogen) following the technical recommendations of the manufacturer. Experiments were performed 48 to 72 h after transfection.

Incubation with chemicals

Further details about chemicals are found in the key resources table. At least 24h after transfection, cells were treated with 10 μg/mL tunicamycin (654380, Millipore) for 1h, 4h, or 24h; 10 μM thapsigargin (Thermo Fisher Scientific, Waltham, MA) for 1h or 4h; 10 μg/mL Brefeldin A (BFA, 350-019-M010, Alexis Biochemicals) for 1h or 4h; 25 μM EN460 (328501, Millipore) overnight; 5 μM GKT 137831 (17764, Cayman) overnight; 2.5 μM AMG’44 (5517, Tocris) overnight; 5 mM N-acetyl-L-cysteine (NAC, A9165, Sigma-Aldrich) for 2 h; 0.4 mM TBHP (C10493A, Invitrogen) for 1h; 10 mM dithiothreitol (DTT, A22066A, Invitrogen) for 10 min; 5 mM diamide (D3648, Sigma-Aldrich) for 10 min; 10 mM DL-buthionine-sulfoximine (BSO) for 2 h; 10 mM glutathione ethyl ester (GSH, 14953, Cayman Chemical) for 1h; 1 μM oligomycin A (15218, Cayman) for 4h; 10 μM BAPTA-AM (B6769, Sigma-Aldrich) overnight; 100nM ISRIB (SML0843, Sigma-Aldrich) overnight or DMSO (D2650, Sigma-Aldrich).

pH of the medium

48 h after cell seeding, the growth medium was collected and kept on ice for 1h. The pH of the medium was measured in triplicate using a pH meter (SevenEasy Mettler Toledo).

Lactate measurement in the medium

24h after cell seeding in standard DMEM growth medium, the medium was replaced with DMEM containing 25 mM glucose and 1% FBS, with or without 5 μM EN460, for 18 h. During the 18-h FBS starvation period, cells were treated with 10 μg/mL tunicamycin for 1h or 4h. Then, the media was collected, centrifuged at 400 rcf for 5 min, filtered using a 0.22-μm filter (Millex®-GS, Millipore), and kept on ice. The L-lactate assay was performed using 10 μL of collected medium in a 96-well plate following the technical recommendations of the manufacturer (600455, Cayman). After 30 min of incubation on a shaker at room temperature, the absorbance at 490 nm was measured using a plate reader (Synergy 4 BioTeck).

Mitochondrial activity

Oxygen consumption in MEFs and HEK293 cells was monitored using the Oxygraph-2k machines (Oroboros Instruments Corp., Austria). Prior to oxygraphy measurements, cells were collected using trypsin, centrifuged at 400 rcf for 5 min, and diluted in DMEM to a concentration of 10^6 cells/mL. 2 mL of intact cells were loaded into each chamber, set to 37°C on the magnetic stirrer. First, basal respiration was measured in the presence of endogenous substrates. Next, 2 μg/mL oligomycin (141829, Abcam) was added to measure uncoupled (non-phosphorylating) oxygen consumption. Then, the stepwise addition of 0.05 μM or 0.5 μM carbonyl cyanide 4-(trifluoromethoxy) phenylhydrazone (FCCP, C2920, Sigma-Aldrich) was performed to reach the maximal oxygen consumption. 0.25 μM antimycin was added to obtain non-mitochondrial oxygen consumption.

Total cellular ATP content

Cells were lysed in CHAPS buffer (10 mM tris pH 7.4, 150 mM NaCl, 1 mM EDTA, 1% CHAPS) supplemented with protease inhibitors (Complete, 11873580001, Roche), and kept on ice. After determination of the protein concentration using the BCA Protein Assay Kit (23225, Pierce™ Thermo Scientific), ATP was measured using the ATP Determination Kit (Molecular Probes, A22066). Luminescence was measured at 390 nm by plate reader following the technical recommendations of the manufacturer.

Flow cytometry

Flow cytometry was carried out using a LSRFortessa flow cytometer (BD Biosciences). Single, live cells were gated using an FSC and SSC dot plot. Mean fluorescence intensity was determined on the gated cells. Data analysis was performed using the BD FACSDiva software.

Free ROS

The following probes were used as follows: CellROX™ Orange (C10493A, Invitrogen) to measure cytoplasmic ROS; MitoSOX™ (M36008, Invitrogen) to measure mitochondrial ROS; and CellROX™ Green (C10444, Invitrogen) to measure nuclear/mitochondrial ROS. Prior to flow cytometry analysis, cells were incubated with 5 μM CellROX for 30 min or 5 μM MitoSOX for 15min, at 37°C. Cells were trypsinized and quenched with 1 mL of DMEM, centrifuged at 400 rcf for 5 min, and resuspended in 350 μL of Hank’s Balanced Salt Solution with calcium and magnesium (HBSS/Ca^{2+}/Mg^{2+}, 14025-092, Gibco) containing 0.1% bovine serum albumin (BSA, A6003, Sigma-Aldrich). Then, the fluorescence signals of CellROX Orange (excitation 545/emission 565 nm), CellROX Green (excitation 508/emission 525 nm) and MitoSOX (excitation 510/emission 580 nm) were measured, and the gates were adjusted using a positive control (0.4 mM TBHP for 1h) and a negative control (5 mM NAC for 2 h).

Mitochondrial membrane potential

Prior to flow cytometry analysis, cells were treated with 40 nM tetramethylrhodamine methyl ester (TMRM, 871370, T668, Invitrogen) for 30 min at 37°C. Cells were trypsinized and quenched with 1 mL of DMEM, centrifuged at 400 rcf for 5 min, and resuspended in 350 μL HBSS/Ca^{2+}/Mg^{2+} containing 0.1% BSA. Then, the fluorescence signals of TMRM (excitation 552/emission 579 nm) was measured and gates adjusted using a positive control (3 μM oligomycin for 2 h) and a negative control (10 μM FCCP for 2 h).

Apoptosis and cell mortality

Media containing the dead cells were collected and attached cells were trypsinized and quenched with 1 mL of DMEM, centrifuged 400 rcf for 5 min, and washed once with the 1× Annexin V binding buffer (10×: 0.1 M HEPES-NaOH pH 7.4, 1.4 M NaCl, 25 mM $CaCl_2$) and centrifuged following the recommendations of the manufacturer (PE-Annexin V-Apoptosis Detection Kit I, 559763, BD Pharmingen^{TM}). Then, cells were resuspended and incubated with Annexin V binding buffer containing 25 μL/mL PE Annexin V probe and 7-Amino-Actinomycin (7-AAD) probe for 15min at room temperature. The fluorescence signals of PE Annexin V probe (excitation 566/emission 574nm) and 7-AAD probe (excitation 546/emission 647nm) were measured. The gates were adjusted using a positive control (10 μg/mL tunicamycin for 24h) and a negative control (5 mM NAC for 2 h), in order to define the different cell subpopulations (Q1, Q2, Q3, and Q4 representing dead, late apoptosis, live and early apoptosis cells, respectively).

Lipid measurements

After 72 h of cell growth in 10-cm dishes, MEFs were trypsinized and quenched with 1 mL of DMEM. Protein concentration was determined using the BCA Protein Assay Kit. Cell suspensions were centrifuged at 400 rcf for 5 min and resuspended in glasses tubes containing 4 mL of choroform:methanol:water (8:4:3) containing 25 μg of phosphatidyl-dimethylethanolamine and 100 μg of butyl alcohol, as internal standards, following a modified version of the Folch technique.[74] Tubes were vortexed for 1 min and centrifuged at 750 rcf for 10 min to separate phases. Then, the bottom, lipid phase was transferred to a new glass tube using the double Pasteur pipette technique. Samples were dried under a stream of nitrogen and resuspended in 50 μL of chloroform:isooctane (1:1) and transferred to HPLC vials (Agilent) containing a glass spring insert and stored at −20°C until analysis.

High performance liquid chromatography (HPLC) was carried out using an Agilent 1100 instrument equipped with a quaternary pump and an Alltech ELSD2000 evaporative light-scattering detector, using a modified version as described.[75] Briefly, the cell homogenate was assayed for protein content, and the homogenate equivalent was extracted using a modified version of the Folch technique (see Part 4.1). Then, 10 μL of chloroform:isooctane (1:1) containing lipids was injected onto the column. Lipids were separated using a three-solvent gradient on a Kinetex 4.6 × 50 mm 2.6-μm HILIC column (Phenomenex), at a flow rate of 1 mL/min 2.6-μmx.

Transmission electronic microscopy

MEFs were washed, fixed, and sectioned for transmission electronic microscopy (TEM) as previously described.[32] Images were taken at 30k magnification. The quantitative analysis of ER length, mitochondria circumference, distance between ER and mitochondria (up to 50 nm), as well as contact number and length of contact, was done using Fiji® (NIH, USA), as previously described.[76] A minimum of 25 pictures were taken per condition, and at least 50 cells were analyzed per group.

Immunofluorescence microscopy

HeLa cells and MEFs were grown on 12-mm coverslips (Fisherbrand^{TM}, Fisher Scientific) previously coated with poly-L-lysine (P4707, Sigma-Aldrich) in 12-well plates, and transfected as previously described. Then, cells were washed twice with 1X PBS++ (10×: PBS with 1 mM $CaCl_2$, 0.5 mM $MgCl_2$, 14200-075, Gibco) and fixed with 4% paraformaldehyde (PFA, 15710, Electron Microscopy Science EMS) for 15min. Cells were washed with PBS++ once and quenched with 50 mM NH_4Cl (in PBS++) for 10 min at room temperature. Next, cells were washed twice with PBS++ and permeabilized with 0.1% Triton X-100 (1086431000, Sigma-Aldrich) + 0.2% BSA (in PBS++) for 2 min under agitation, and washed again with PBS++ before blocking with 0.2% saponin (47036, Sigma-Aldrich) + 2% BSA (in PBS++) for 10 min. Then, cells were incubated with primary antibodies (PERK rabbit: 65142, Abcam at 1:50; ERO1α mouse: MABT376, Millipore, at 1:50) for at least 1h at room temperature in a light-protected, humid chamber. Cells were washed once with wash buffer (PBS++ containing 0.1% Triton X-100 + 0.2% BSA) for 2 min, and 3 times with PBS++ for 5 min, under agitation. Then, the cells were incubated with secondary antibodies (goat anti-IgG-Rabbit 594 (Red) A11012 and goat anti-IgG2a-Mouse 488 (Green) A21131 from Invitrogen, AlexaFluor, 1:1000) for at least 30 min. Cells were washed once with wash buffer and 3 times with PBS++. Finally, coverslips were mounted using VECTASHIELD® PLUS Antifade Mounting Medium reagent (MJS-Biolynx inc., # VECTH19002). Pictures were acquired with the Zeiss Observer Z1 inverted phase contrast fluorescence microscope (Axiocam), equipped with a 100× objective. Iterative deconvolution was performed with the Axiovision software (40 V4.8.0.0). For co-localization analyses, Mander's Overlap Coefficient was calculated with Fiji® software (NIH, USA). A minimum of 10 images were analyzed per sample.

Mitochondria Morphology

Morphology of the mitochondrial network was quantified using the MitoTracker^{TM} Red CMXRos fluorescent probe (M7512, ThermoFisher). Cells were incubated with 100 nM MitoTracker^{TM} for 30 min at 37°C. Then, cells were fixed, mounted, and imaged as previously described. The mean area, perimeter, and major and minor radii of mitochondria was measured using Fiji® (NIH, USA).[76] Mitochondrial fusion and fission was evaluated using the parameters form factor (FF = 4π × area/perimeter[2]) and aspect ratio (AR = major radius/minor radius).[77] A minimum of 10 images were analyzed per sample, and 3 independent experiments were performed for each treatment.

SPLICS measurement of MERCs

MEFs were seeded on 12-mm coverslips previously coated with poly-L-lysine in 12-well plates. After 1 day, cells were transfected with SPLICS (Long and Short) plasmids. Media was replaced 24h post-transfection with DMEM containing 25 μM EN460 or DMSO. 24h later, cells were treated with tunicamycin or DMSO for 1h. Then, the cells were fixed and mounted. Images were acquired in 0.25 μM stacks using Zeiss Observer Z1 inverted phase contrast fluorescence microscope equipped with a 100× oil-immersion objective. Images were deconvolved using the Huygens Professional Deconvolution Software (Version 20.04, Scientific Volume Imaging). Prior to analysis, pictures were processed using Fiji® software (NIH, USA) as previously described.[46,78]

PLA assessment

MEFs were seeded on 12-mm coverslips previously coated with poly-L-lysine in 12-well plates. After 1 day, cells were transfected with pcDNA4-GFP-P2A-FATE1 or pcDNA4 plasmids (see Part 1.1). Media were replaced 24h post-transfection with DMEM containing 25 μM EN460 or DMSO. 24h later, cells were treated with tunicamycin or DMSO for 1h. Cells were fixed, permeabilized, blocked and incubated overnight at 4°C with a binary mixture of anti-IP$_3$R1 (1/300 dilution, Millipore #3809289) and VDAC1 (1/300 dilution, Abcam #14734) primary antibodies. The second day, after two washes with TBS-T (tris-buffered saline - 0,05% Triton), cells were incubated with the complementary secondary antibody (rabbit PLUS: #DUO92002 and mouse MINUS: #DU092004, SigmaAldrich) for 1h at 37°C in a pre-heated humidity chamber. Cells were washed. Then the proximity ligations and the polymerase amplifications were then performed using the reagent and the instruction of the manufacturer (SigmaAldrich, Duolink®, #DU092008). Nuclei were stained using DAPI (4′,6-diamidino-2-phenylindole) incubation for 5min in pre-heated humidity chamber. Cells were washed again, and preparations were mounted using VECTASHIELD® PLUS Antifade Mounting Medium reagent (MJS-Biolynx inc., # VECTH19002). Images were acquired in 0.25 μM stacks using Zeiss Observer Z1 inverted phase contrast fluorescence microscope equipped with a 100× oil-immersion objective. Images were deconvolved and a Gaussian filter was applied using the Fiji® software (NIH, USA) prior to analysis the number of dots/nucleus as previously described.[79,80]

Live cell measurements

MEFs of HeLa cells were seeded on 12-mm coverslips previously coated with poly-L-lysine in 12-well plates. At time of imaging, cells were at approximately 80% confluency. Live imaging was conducted with an Olympus FV1000 laser-scanning confocal microscope equipped with a 20× objective (XLUMPLANFL, NA 1.0, Olympus). Images were acquired using the Olympus FluoView software and analyzed with Time Series Analyzer v3.0 plugin on Fiji® software (NIH, USA), as previously described[32,73] for the calcium data (ER-GECO, Mito-RGECO and Fluo-8L AM),[42] for the ERroGFP2 data,[71] for the ERAT4.01 and a recently submitted BioRxiv manuscript for the L-lactate iLACCO1.2 imaging data.

ER Ca^{2+} measurements

To measure ER Ca^{2+}, the ER-RGECO (LAR-ER-GECO,[48] was used. After 24h of overexpression of ER-RGECO and application of specific treatments in MEFs, coverslips were transferred to the microscope chamber containing HBSS/Ca^{2+}/Mg^{2+}. Then, cells were perfused with HBSS/Ca^{2+}/Mg^{2+} at a flow rate of 5 mL/min for the first 30 s using a perfusion system pump (Watson-Marlow Alitea-AB, Sin-Can) to establish the baseline fluorescence. Then, cells were perfused with HBSS supplemented with 1.75 μM $MgCl_2$ (MX0045-1, EM Science), 410 μM $MgSO_4$ (230391, Sigma-Aldrich), 100 μM EGTA (4100, OmniPur EMD), and 60 μM tert-butylhydroquinone (TBHQ, 97%, 112941, Sigma-Aldrich) for 14.5 min at room temperature, to block SERCA pump activity and quantify the clearance of calcium from the ER. Images were taken every 3 s in the Alexa 546 channel (559-nm laser excitation and a 575- to 675-nm bandpass emission filter).

Mitochondrial Ca^{2+} measurements

To measure the mitochondrial Ca^{2+}, mitochondrial R-GECO (Mito-RGECO,[48] was used. After 24h of overexpression of Mito-RGECOand application of specific treatmentsin HeLa cells or MEFs, coverslips were transferred to the microscope chamber containing HBSS/Ca^{2+}/Mg^{2+}. After establishing the baseline fluorescence, the cells were perfused with HBSS/Ca^{2+}/Mg^{2+} or with HBSS without calcium supplemented with 1.75 μM $MgCl_2$, 410 μM $MgSO_4$, 100 μM EGTA, 10 μM FCCP (15218, Cayman) for 12 min; with HBSS/Ca^{2+}/Mg^{2+} containing 600 μM ATP (A2383, Sigma-Aldrich) for 4 min; or with HBSS/Ca^{2+}/Mg^{2+} containing 10 μg/mL tunicamycin for 13 min at room temperature. Live cell images were taken every 5 s during the FCCP treatment and every 1 s during the ATP and tunicamycin treatments, in the Alexa 546 channel (559-nm laser excitation and a 575- to 675-nm bandpass emission filter).

Cytoplasmic Ca^{2+} measurements

After application of specific treatments, MEFs were treated with 3 μM Fluo-8L AM (21097, AAT Bioquest) for 30 min at 37°C and transferred to the microscope chamber containing HBSS/Ca^{2+}/Mg^{2+}. After establishing the baseline fluorescence, the cells were perfused with HBSS/Ca^{2+}/Mg^{2+} containing 600 μM ATP for 4 min at room temperature. Live cell images were taken every 1 s in the Fluo-4 channel (473-nm laser excitation with a 490- to 540-nm bandpass emission filter).

L-lactate measurements

To measure the mitochondrial cytoplasmic L-lactate in MEFs, iLACCO1.2 (submitted to BioRxiv) was used. Indicators was based on green fluorescent proteins. After 24h of overexpression of iLACCO1.2 and application of specific treatments, cells were transferred to the microscope chamber containing HBSS/Ca^{2+}/Mg^{2+}. After establishing the baseline fluorescence, the cells were perfused with HBSS/Ca^{2+}/Mg^{2+} containing 10 μg/mL tunicamycin for 14-15min at room temperature. Live cell images were taken with the TimeScan set as FreeRun mode with 800 pictures acquisition in the EGFP channel (473-nm laser excitation with a 490- to 540-nm bandpass emission filter). The absence of pH changes was assayed with pHuji.[81]

ER redox poise measurements

To measure the ER redox poise in MEFs, ERroGFP2 was used. After 24h of overexpression of ERroGFP2 and application of specific treatments, cells were transferred to the microscope chamber containing HBSS/Ca^{2+}/Mg^{2+}. After establishing the baseline fluorescence, the cells were perfused with HBSS/Ca^{2+}/Mg^{2+} containing 10 μg/mL tunicamycin for 13 min, DTT (10 mM) for 4 min and diamide (5 mM) for 4 min at room temperature. Live cell images were taken with the TimeScan set as FreeRun mode with 105 pictures acquisition (interval: 2 sec.). Images were acquired upon excitation at 405 nm and 488 nm with speed set at 8 μs/pixel and using the laser lines mode. The spectral setting was set to 500–600 nm and pictures were acquired with separation of the two channels in sequential frame mode using Kalman filter mode (with 405/488 Excitation DM and SDM 490 for each channel) The ratio is calculated by divided the intensity from the channels excited at 405 nm by the intensity from the channels excited at 480 nm after subtracted background in each channel.

ER-ATP measurements

To measure the ER-ATP in MEFs, the FRET-based ERAT4.01 was used. After 24h of overexpression of ERAT4.01 and application of specific treatments, cells were transferred to the microscope chamber containing HBSS/Ca^{2+}/Mg^{2+}. After establishing the baseline fluorescence, the cells were perfused with HBSS/Ca^{2+}/Mg^{2+} containing 10 μg/mL tunicamycin for 13–14 min at room temperature. Live cell images were taken with the TimeScan set as FreeRun mode with 331 pictures acquisition. Images were acquired with CFP/YFP FRET mode (458 nm laser excitation with a 475–500 nm and 515–615 nm bandpass emission filters). The ratio is calculated by divided the intensity from the emission channel 515–615 nm by the intensity from the emission channel at 475–500 nm after subtracted background in each channel.

Hydrogen peroxide measurements

MEF PERK WT or MEF PERK ko cells, seeded on 25 mm round (No 1.5, #6310172, VWR) glass coverslips (150,000–170,000) were transfected after 24h with 1 (for OMM-HyPer (pCMV_pL4_AKAP1_HyPer_DAAO)/OMM-SypHer (pCMV_pL4_AKAP1_SypHer_DAAO) plasmid, 3 μL Lipofectamine2000 (#11668027, Thermo Fisher Scientific GmbH, Schwerte, Germany) and 100 μL OptiMEM (#51985034, Thermo Fisher Scientific GmbH, Schwerte, Germany) 24h prior imaging according to manufacturer's instructions. Cells were pre-treated with 25 μM EN460 or DMSO overnight and additional treatment of 10 μg/mL tunicamycin (or DMSO) was added 1h before imaging. The measurements were performed in Ringer's buffer (pH 7.4) containing 145 mM NaCl, 4 mM KCl, 10 mM Glucose, 10 mM HEPES (4-(2-hydroxyethyl)-1-piperazineethanesulfonic acid), 2 mM $MgCl_2$ and 0.5 mM $CaCl_2$. Experiments were performed with a Zeiss Observer D1 equipped with a 40x EC-Plan Neofluar (N.A. 1.3) oil objective, Axiocam 702 mono and LED system (Colibri, Zeiss) at 37°C. Images were acquired upon excitation at 420 nm (excitation filter: 420/40) and 505 nm (excitation filter: 500/15) together with a 515 nm dichroic mirror and 539/25 emission filter. Data were analyzed using Zen 2.6 software (Carl Zeiss Microscopy GmbH, Oberkochen, Germany).[82]

Western blot

Cell lysates were prepared using in RIPA+ lysis buffer (RIPA buffer (50 mM Tris-HCl pH 7.4, 150 mM NaCl, 5 mM MgCl2, 1% NP-40, 0.25% sodium deoxycholate), supplemented with protease inhibitors (Complete, 11873580001, Roche) and phosphatase inhibitors (4693159001, Roche)). Samples were vortexed and centrifuged at 13,000 rcf for 15min to remove nuclei and unbroken cells. Protein concentration was determined using the BCA Protein Assay Kit. 15 to 30 μg of protein was diluted in 5× sample loading buffer (60 mM tris-HCl pH 6.8, 2% SDS, 10% glycerol, 10% β-mercaptoethanol, 0.004% bromophenol blue) and denatured at 75°C for 10 min. Protein samples were subjected to SDS-polyacrylamide gel electrophoresis at 150 V. Then, proteins were transferred onto nitrocellulose membranes for 2 h at 4°C at 400 mA. After, membranes were blocked in blocking buffer (10 mM tris pH 8, 150 mM NaCl, 0.05% Triton X-100, 2% BSA or milk) for at least 30 min. Then, membranes were incubated in primary antibodies (diluted at 1:1000 and listed in the key resources table) overnight. Membranes were washed 3 times with washing buffer (10 mM tris pH 8, 150 mM NaCl, 0.05% Triton X-100) and incubated in secondary antibodies (diluted at 1:10000 and listed in the key resources table) for at least 1h. Membranes were washed 3 times and scanned using an Odyssey scanner (Version 1.1, LI-COR). Quantification was determined using the ImageLab software (Biorad). **Non-reducing gels:** Cell lysates were prepared as previously described (see Part 6.1), with or without 20 mM N-ethylmaleimide (NEM, E-3876, Sigma-Aldrich). Additionally, protein samples were diluted in 5× sample loading buffer free of β-mercaptoethanol and subjected to SDS-polyacrylamide gel electrophoresis without boiling.

Co-immunoprecipitation

Cells were grown to confluency in at least one 10-cm dish per condition. Cells were washed with PBS++ and incubated for 30 min at room temperature with 2 mM dithiobis succinimidyl propionate (DSP, 22585, Thermo-Scientific) in PBS++ containing protease phosphatase inhibitors (see 6.1). Then, samples were washed again with PBS++ and quenched with 10 mM of NH_4Cl (A9434, SigmaAldrich) at room temperature for 10 min. Samples were washed with PBS++ and resuspended in 300 μL RIPA+ lysis buffer. Cell lysates were vortexed and centrifuged at 13,000 rcf for 15min to remove nuclei and unbroken cells. 25 μL of the supernatant was set aside as the input at −20°C, and the rest was incubated overnight with primary antibodies or anti-Flag M2 magnetics beads (M8823, SigmaAldrich) at 4°C on a rocker. The following day, samples were incubated with Dynabeads^{TM} Protein A magnetics beads (10002D, Invitrogen) for at least 1h at 4°C on a rocker. The beads were washed at least 5 times for at least 1h with RIPA+ lysis buffer, then resuspended in 24 μL of 2× sample loading buffer. Input samples were diluted in 5× sample loading buffer. Samples were boiled at 75°C for 10 min. 22 μL of co-IP and 10 μL of input samples were subjected to SDS–polyacrylamide gel electrophoresis and western blot.

Mass spectrometry

After immuno-precipitation of PERK (6,4mg of protein/sample) using Flag-magnetics beads (see part. 6.2), beads were washed 3 times in Milli-Q water. Afterward, proteins were reduced (DTT) and alkylated (iodoacetamide). Then, beads and proteins were separated by Thermo Kingfisher equipment by on-bead digestion using trypsin (at 1μg in 100μL of 50 mM ammonium bicarbonate). The follow day, the reaction was quenched (by Formic Acid at 2%) and desalted (by C18 ZipTip) before to be analyzed in LC–MS/MS onto a C18 reverse-phase column.[83]

Protein redox state

Per condition, cells were seeded in 3 wells of a 6-well plate. At least 24h post-transfection of PERK-Flag, IP$_3$R1-HA or SERCA-Myc, cells were incubated with specific treatments, or with 10 mM DTT and 5 mM diamide, constituting the fully reduced and oxidized controls, respectively, for 10 min at 37°C. Cells were washed with PBS++ and lysed with 45 μL of 200 μM biotin-iodoacetamide (BIAM, 21334, Thermo Scientific) reaction buffer (50 mM tris-HCl pH 8, 50 mM NaCl, 5 mM EDTA, 1% Triton X-100, 0.1% IGEPAL (CA-630)) containing protease inhibitors (Complete, 11873580001, Roche), per well. Then, 3 wells per condition were pooled and centrifuged at 10,000 rcf for 5 min. The supernatant was collected and kept in the dark for 90 min at room temperature to allow the biotinylation of reduced proteins. Bio-Spin columns (732–6221, Bio-Rad) were washed at least 3 times with CHAPS buffer and once with CHAPS buffer containing complete protease inhibitors. To remove the unreacted BIAM, each sample was loaded into two Bio-Spin columns and centrifuged at 1,000 rcf for 4 min. Then, samples were incubated overnight with 4 μL of antibodies (Flag: F7425, Sigma-Aldrich, Cell-Signaling; HA: C29F4, Cell-Signaling; Myc: 13–2500, Invitrogen). The following day, proteins were precipitated. Beads were washed at least 5 times for 1h with CHAPS buffer. Samples were diluted in 2× sample loading buffer containing 50 mM DTT and boiled at 75°C for 10 min. Samples were subjected to SDS–polyacrylamide gel electrophoresis and transferred to a nitrocellulose membrane. Membranes were incubated overnight with the goat anti-α-Biotin primary antibody (B3640, Sigma-Aldrich) and anti-Flag, HA, or Myc antibodies the following day.

Subcellular fractionation

Subcellular fractionation was conducted as previously described.[84] MEFs were grown to confluency in fifteen 20-cm dishes per condition and resuspended in 7.5 mL of homogenization buffer (0.25 M sucrose, 10 mM HEPES-NaOH pH 7.4, 1 mM EDTA, 1 mM EGTA) supplemented with protease inhibitors (Complete, 11873580001, Roche) and phosphatase inhibitors. Cells were spun down at 300 rcf for 5 min at 4°C using a JA-12 rotor (J2-21M, Beckman) and resuspended in 4 mL of homogenization buffer. Then, cells were homogenized using a ball-bearing homogenizer (Isobiotec, Heidelberg, Germany, ball clearance 18 μm). Cells were passed at least 10 times through the homogenizer, then centrifuged at 600 rcf for 10 min at 4°C using a JA-12 rotor to yield the homogenate fractions. A portion of the homogenate was diluted in RIPA+ buffer and stored at −80°C, and the rest was centrifuged at 10,300 rcf for 10 min at 4°C using a JA-12 rotor to yield the crude mitochondria fractions (pellet). The supernatants were then centrifuged at 60,000 rpm for 1h at 4°C using a TLA 120.2 rotor (Coulter Optima^{TM}-MAX-XP Centrifuge, Beckman) to obtain the microsome fractions (pellet) and cytosolic fractions (supernatant). Each crude mitochondria fraction was resuspended in 1 mL of homogenization buffer containing inhibitors and layered on 7.9 mL of homogenization buffer containing 18% Percoll (17-0891-02, GE Healthcare) in Coulter centrifuge tubes (361623, Beckman). The crude mitochondria fractions were then centrifuged at 95,000 rcf for 35 min at 4°C using a 90Ti rotor (Beckman Coulter 259051) to obtain the MAM fractions (upper band) and mitochondria fractions (lower band). The MAM fractions were centrifuged at 60,000 rpm for 1h at 4°C using a TLA 120.2 rotor, and the pellet obtained was resuspended in RIPA+ buffer. The mitochondria fractions were centrifuged at 10,000 rcf (S415R, Eppendorf) for 10 min at 4°C, then resuspended in homogenization buffer and centrifuged again at 10,000 rcf for 10 min at 4°C. The pellet was resuspended in RIPA+ buffer. The cytosolic fractions were precipitated with cold acetone (A18-1, Fisher Chemical) overnight at −20°C. The following day, the cytosolic fractions were centrifuged at 16,100 rcf (S415R, Eppendorf) for 20 min, and the pellets were resuspended in RIPA+ buffer. The protein concentration of each fraction was determined using the BCA Protein Assay Kit, and 15 μg of protein was analyzed by western blot.

Heavy and light membrane fractionation

Subcellular fractionation was previously published.[43] Cells were grown to confluency in one 10-cm dish per condition. Cells were washed with PBS++ and resuspended in 600 μL of homogenization buffer containing protease inhibitors (Complete, 11873580001, Roche) and phosphatase inhibitors. Then, cells were homogenized using a ball-bearing homogenizer. Cell homogenates were centrifuged at 800 rcf (S415R, Eppendorf) for 10 min at 4°C to remove nuclei and unbroken cells. Then, the supernatants were centrifuged at 10,000 rcf for 10 min (S415R, Eppendorf) at 4°C. The pellets were resuspended in 60 μL of RIPA+ buffer to yield the heavy membrane (HM) fractions. The supernatants were centrifuged at 60,000 rpm for 1h at 4°C using a TLA 120.2 rotor. The pellets were resuspended in 60 μL of RIPA+ buffer to yield the light membranes (LM) fractions. The protein concentration of each fraction was determined using the BCA Protein Assay Kit, and 15 μg of protein was analyzed by western blot.

QUANTIFICATION AND STATISTICAL ANALYSIS

All data is presented as mean ± standard error of the mean (SEM). p values < 0.05 were considered significant. After verification of data normality (using Shapiro-Wilk or Agostino & Pearson omnibus normality test) and homogeneity (using Bartlett's test), one-way or two-way analysis of variance (ANOVA) was performed to test the effects of the experimental conditions. When a significant effect was detected, a posteriori Bonferroni correction or Fisher test was used to analyze pairwise differences. For comparison between two groups, data were analyzed with Kruskal Wallis or Student's t-test. Statistical analysis was performed using GraphPad Prism® software (USA).